Chem

CellPress
OPEN ACCESS

Article

Covalent bicyclization of protein complexes yields durable quaternary structures

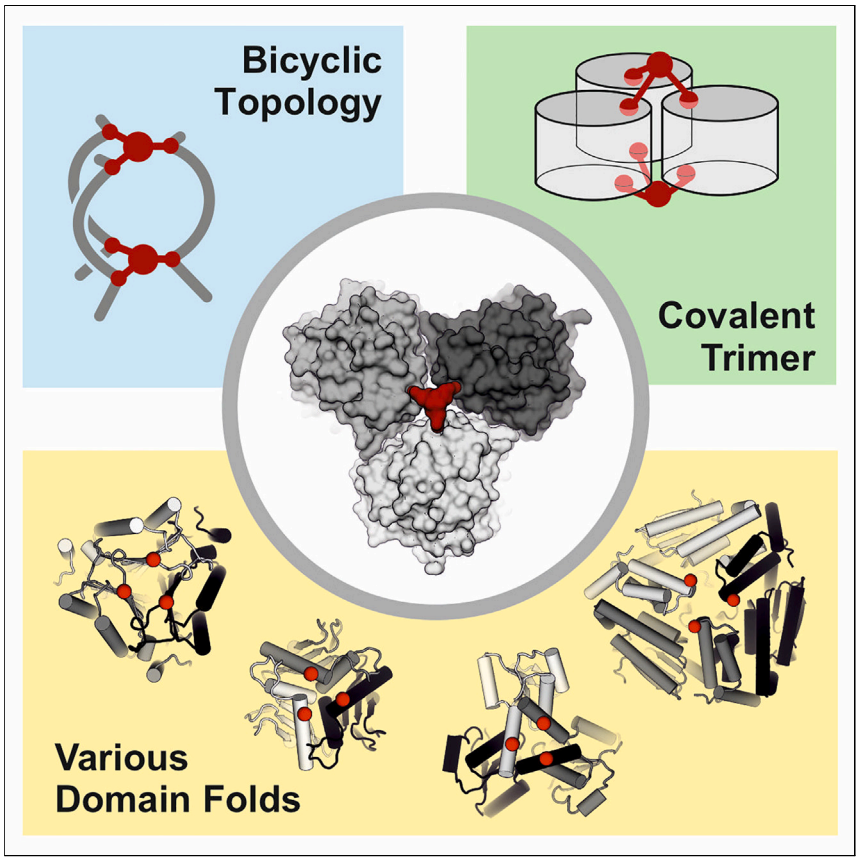

Modulating the stability of protein complexes is crucial for their use in biotechnological applications, such as biocatalysis, offering more sustainable alternatives to traditional chemical transformations. Protein stabilization is typically a labor-intensive process, reliant on extensive screening. Here, we apply a structure-based approach, which utilizes three-pronged reactive cross-linkers to chemically modify and tether a diverse range of trimeric protein complexes. The resulting abiological and cyclic chain connectivity offers robust enzymatic activity and complex stability under challenging thermal and chemical conditions.

George H. Hutchins, Sebastian Kiehstaller, Pascal Poc, ..., Saskia Neubacher, Sven Hennig, Tom N. Grossmann

saskia@incircular.com (S.N.)
s.hennig@vu.nl (S.H.)
t.n.grossmann@vu.nl (T.N.G.)

Highlights

Triselectrophiles cross-link homotrimeric proteins, forming bicyclic topologs

Bicyclic enzyme exhibits activity under denaturing conditions

Approach is rapidly applicable to a structurally diverse range of complexes

Hutchins et al., Chem *10*, 615–627
February 8, 2024
Published by Elsevier Inc.
https://doi.org/10.1016/j.chempr.2023.10.003

Chem

CellPress
OPEN ACCESS

Article

Covalent bicyclization of protein complexes yields durable quaternary structures

George H. Hutchins,[1,2,5] Sebastian Kiehstaller,[3,5] Pascal Poc,[1] Abigail H. Lewis,[1] Jisun Oh,[1] Raya Sadighi,[1,2] Nicholas M. Pearce,[1,2,4] Mohamed Ibrahim,[1] Ivana Drienovská,[1,2] Anouk M. Rijs,[1,2] Saskia Neubacher,[3,*] Sven Hennig,[1,2,*] and Tom N. Grossmann[1,2,6,*]

SUMMARY

Proteins are essential biomolecules and central to biotechnological applications. In many cases, assembly into higher-order structures is a prerequisite for protein function. Under conditions relevant for applications, protein integrity is often challenged, resulting in disassembly, aggregation, and loss of function. The stabilization of quaternary structure has proven challenging, particularly for trimeric and higher-order complexes, given the complexity of involved inter- and intramolecular interaction networks. Here, we describe the chemical bicyclization of homotrimeric protein complexes, thereby increasing protein resistance toward thermal and chemical stress. This approach involves the structure-based selection of cross-linking sites, their variation to cysteine, and a subsequent reaction with a triselectrophilic agent to form a protein assembly with bicyclic topology. Besides overall increased stability, we observe resistance toward aggregation and greatly prolonged shelf life. This bicyclization strategy gives rise to unprecedented protein chain topologies and can enable new biotechnological and biomedical applications.

INTRODUCTION

Proteins represent a versatile molecular platform, essential to life on earth and a rich source of inspiration for the development of novel biotechnological tools.[1–5] Self-association of proteins into homomeric complexes is widespread, facilitating an evolutionarily relevant increase in morphological complexity.[6] However, applications such as catalysis in abiotic environments often involve extreme conditions that challenge the structural integrity of proteins and disrupt complex assemblies. Although considerable efforts have enhanced the thermal and chemical stability of protein folds (tertiary structure),[7–11] the stabilization of protein complexes and their supramolecular assembly (quaternary structure) remains a challenge. Such approaches have mainly focused on homodimeric protein complexes. For example, homodimeric isologous interfaces (in which each interaction surface is identical)[12] have been stabilized or artificially engineered via systematic mutagenesis[13] and computational approaches.[14,15] The introduction of inter-molecular disulfide bridges or non-canonical amino acids, and the design of fusion proteins, have been utilized to covalently link monomer units within dimeric complexes.[16–20] In contrast, many higher-order complexes, such as homotrimers, possess heterologous interfaces (i.e., where the interacting surfaces differ), which present a bigger challenge for engineering due to the inherent necessity for more mutations and the risk of rearrangement into polymeric aggregates.[21] General approaches toward the efficient stabilization of these complexes are currently lacking.

THE BIGGER PICTURE

The cyclization of small molecules, peptides, and macromolecules is a fundamental strategy to design precise three-dimensional molecular shapes tailored to chemical function. Proteins, however, typically consist of linear polypeptide strands, where protein folding and assembly are governed by non-covalent interactions. Protein engineering to form precise interlinked and cyclized protein chains has the potential to expand the biotechnological applications of proteins beyond their natural environments. Here, we construct a covalent bicyclic enzyme, capable of withstanding an exceptional degree of chemical and thermal stress. Such molecules can offer new avenues for sustainable industrial chemistry and biocatalysis, functioning in chemical environments that were previously inaccessible with biological components.

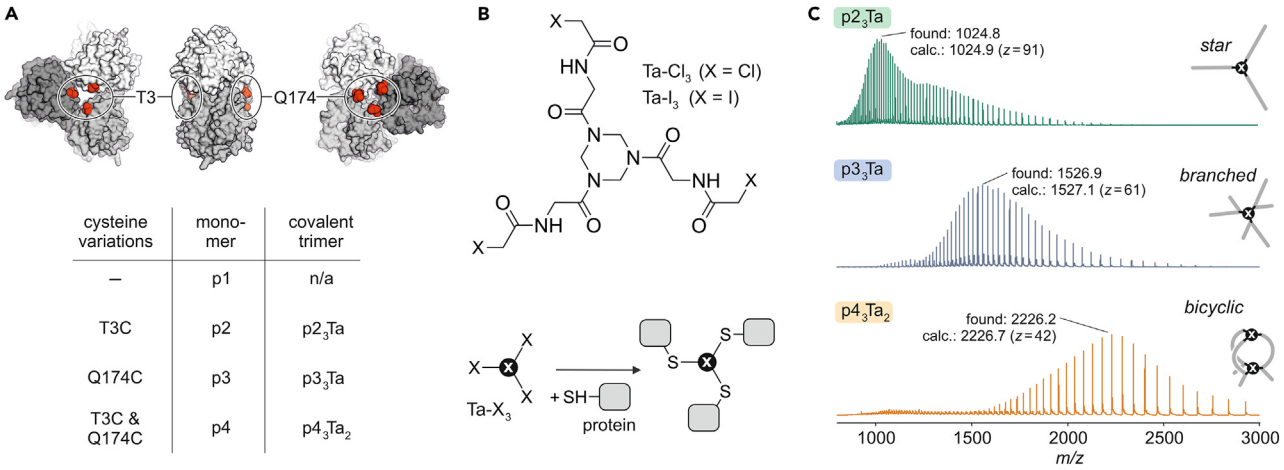

Figure 1. Covalent multimerization and bicyclization

(A) Crystal structure of *Pseudomonas fluorescens* esterase (**p1**, PDB: 1va4), including modification sites (red, T3, and Q174) with amino acid variations and corresponding protein (and complex) names. For sequences and design details see Figure S1.

(B) Cysteine-selective cross-linking using chloroacetamide or iodoacetamide-based cross-linkers (Ta-Cl_3, Ta-I_3).

(C) Scheme of trimer chain topology. Mass spectra (ESI-TOF) of cross-linked protein trimers including the charge state of the most abundant signal (see Tables S2–S5 for complete lists of MS signals).

Bioconjugation strategies have emerged as powerful techniques to enhance and alter protein functionality, providing access to powerful labeling tools, screening platforms, and novel therapeutic entities, such as antibody-drug conjugates.[22–24] The use of bioconjugation approaches for protein structure stabilization is uncommon, and has focused on either tertiary structure stabilization[25–27] or inter-chain cross-linking to trap weak complexes and probe for unknown protein-protein interactions.[28–30] Herein, we aimed to employ biocompatible, multivalent modifiers for the stabilization of protein complexes. We have previously reported the *in situ* cyclization of proteins (INCYPRO) for the stabilization of tertiary structures,[26,27,31] which utilizes C3-symmetric triselectrophiles[32–34] that react with three spatially aligned cysteine side chains on the protein surface. Given the C3 symmetry of protein homotrimers, we considered whether it is possible to cross-link homotrimeric complexes with these triselectrophiles, thereby constructing protein conjugates with high tolerance toward thermal and chemical stress. Our approach aimed to fundamentally alter the chain topology of trimeric complexes, converting three protein monomers into a single, covalently interlinked chain with bicyclic topology. This enabled the construction of a stress-resistant enzyme capable of catalysis under denaturing conditions. To further challenge the concept, we explored a suite of structurally diverse trimeric complexes, successfully generating a range of stabilized trimeric complexes and obtaining four additional precisely bicyclized protein trimers with substantially increased thermal stability.

RESULTS AND DISCUSSION

Construction of covalently cross-linked protein trimers

We initially selected *Pseudomonas fluorescens* esterase (PFE) as a target for complex stabilization. PFE is a well-characterized homotrimeric hydrolase, which has served previously as a platform for protein engineering efforts.[35,36] Based on an earlier reported crystal structure of PFE (Protein Data Bank; PDB: 1va4),[37] we searched for cross-linking sites on the two faces of the trimer (Figure 1A) to enable covalent linkage by a triselectrophile (Figure 1B). Given the C3-symmetry of the PFE complex, the variation of a single residue results in three equivalent modified sites per trimer. We considered suitable Cα–Cα distances of 8–15 Å (Figure S1) between modified residues and identified two solvent

[1]Department of Chemistry and Pharmaceutical Sciences, Vrije Universiteit Amsterdam, 1081 HZ Amsterdam, the Netherlands

[2]Amsterdam Institute of Molecular and Life Sciences, Vrije Universiteit Amsterdam, 1081 HZ Amsterdam, the Netherlands

[3]Incircular B.V., 1081 HZ Amsterdam, the Netherlands

[4]Department of Physics, Chemistry and Biology, SciLifeLab, Linköping University, 581 83 Linköping, Sweden

[5]These authors contributed equally

[6]Lead contact

*Correspondence: saskia@incircular.com (S.N.), s.hennig@vu.nl (S.H.), t.n.grossmann@vu.nl (T.N.G.)

https://doi.org/10.1016/j.chempr.2023.10.003

exposed residues (T3 and Q174) close to the central C3 axis as potential cross-linking sites (Figure 1A). Cysteine residues were introduced to the wild-type enzyme (denoted **p1**) at these two positions, furnishing two variants for mono-cross-linking (**p2**, T3C; **p3**: Q174C) and one for bis-cross-linking, combining both variations (**p4**, Figure 1A). Notably, the latter generates an interlinked bicyclic topology upon modification. The selected variation sites are distant from the catalytic pocket and therefore not expected to directly interfere with enzymatic activity (Figure S1). Each PFE monomer bears one native cysteine which is, however, buried and not accessible for electrophilic modification.

The chemical cross-linking of the PFE variants was initially pursued with the chloroacetamide bearing triselectrophile *N*,*N*′,*N*″-((1,3,5-triazinane-1,3,5-triyl)tris(2-oxoethane-2,1-diyl))tris(2-chloroacetamide) (Ta-Cl_3) (Figure 1B) and analyzed using sodium dodecyl sulfate (SDS) polyacrylamide gel electrophoresis (PAGE). We observed only limited reactivity, however (Figure S2), particularly for variant **p2** (T3C), failing to form detectable levels of product. To address this issue, we envisioned the use of a more reactive triselectrophilic cross-linker, retaining the triazinane core but replacing chloroacetamide with the more reactive and cysteine-specific iodoacetamide. The corresponding cross-linker *N*,*N*′,*N*″-((1,3,5-triazinane-1,3,5-triyl)tris(2-oxoethane-2,1-diyl))tris(2-iodoacetamide) (Ta-I_3) (Figure 1B), was obtained via the Finkelstein reaction, employing Ta-Cl_3 and NaI (see experimental procedures).

SDS-PAGE indicated the formation of a defined covalently linked multimeric species for each of the variants (**p2**, **p3**, and **p4**) upon incubation with Ta-I_3 (Figure S3). Interestingly, all cross-linked variants showed a slower mobility than expected for their molecular weight (MW = 90 kDa, apparent MW = 100–150 kDa, Figure S3), which we suspected to be due to their unusual chain topology (Figure 1C). The terminally linked **p2$_3$Ta** exhibits an extended star-like topology, whereas **p3$_3$Ta** is cross-linked via a central cysteine (C174), resulting in a branched topology. Trimer **p4$_3$Ta$_2$** is cross-linked by two entities and therefore forms a compact bicyclic structure. To further analyze the reaction products, high-resolution mass spectrometry (MS) was performed confirming the formation of the expected covalently linked trimers: mono-cross-linked **p2$_3$Ta** and **p3$_3$Ta**, as well as bis-cross-linked **p4$_3$Ta$_2$** (Table S1).

We subsequently performed time-of-flight (TOF) MS under denaturing conditions. The resulting spectra revealed a distinct distribution of charged states for each covalent protein trimer (Figure 1C; Tables S2–S4). The N-terminally linked, star-shaped **p2$_3$Ta** experiences extensive protonation (z(max) = 91, ca. 30 charges per monomer), with an average protonation per monomer comparable to the three unmodified variants (ca. 37 charges, Table S5). Branched **p3$_3$Ta** exhibits reduced protonation levels (z(max) = 61, ca. 20 charges per monomer). This trend continues for the presumably most compact bicyclized trimer **p4$_3$Ta$_2$** (Figure S4), resulting in a considerably lower number of charges (z(max) = 42, ca. 14 charges per monomer). Analogous behavior is observed in SDS-PAGE (Figure S3) where the three covalent trimers show subtle differences in mobility (migration **p4$_3$Ta$_2$** > **p3$_3$Ta** > **p2$_3$Ta**), again suggesting the highest degree of compactness for bicyclic **p4$_3$Ta$_2$** in the unfolded state.

Robust catalysis by triselectrophile-linked enzyme complexes

We next investigated the impact of cross-linking on thermal stability using differential scanning fluorimetry (DSF), revealing enhanced stability for all cross-linked variants when compared with their unmodified precursors (Figure 2A). The most pronounced improvement was observed for bicyclic **p4$_3$Ta$_2$** (ΔT_i = 8.4°C). In addition, we tested

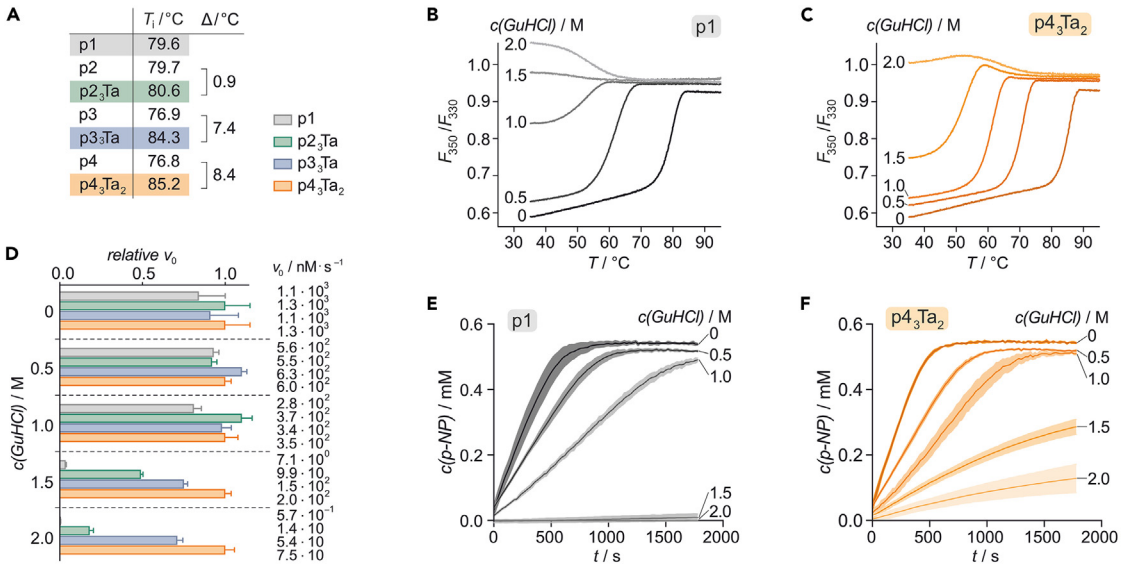

Figure 2. Cross-linking increases protein stability and enzymatic activity under stress

(A) Melting temperatures (T_i) of unreacted and cross-linked variants.

(B and C) Thermal denaturation profiles of **p1** and **p4$_3$Ta$_2$**, respectively, in the presence of varying concentrations of guanidine hydrochloride (GuHCl). For thermal denaturation curves of **p2**, **p3**, **p4**, **p2$_3$Ta**, and **p3$_3$Ta** see Figure S5.

(D) Relative initial rates of enzymatic reaction for **p1** and the three covalent trimers (relative to initial rate of **p4$_3$Ta$_2$** at the given GuHCl concentration). The absolute value for each initial rate is provided (for details see Table S7). The errors account for 1σ (n = 3).

(E and F) Reaction course of substrate conversion by **p1** and **p4$_3$Ta$_2$** in the presence of varying concentrations of GuHCl. For activity curves of **p2**, **p4**, **p4**, **p2$_3$Ta**, and **p3$_3$Ta** see Figure S6. All activity measurements were performed with 2 nM PFE trimer (50 mM HEPES, 50 mM NaCl, pH 7.5). The errors account for 1σ (n = 3).

protein resistance toward chemical stress, employing guanidine hydrochloride (GuHCl) as a chaotropic denaturant. For all proteins, we observed decreasing T_i values with increasing GuHCl concentrations in line with the expected increased unfolding propensity under increasingly chaotropic conditions (Figure S5; Table S6). The sensitivity toward GuHCl, however, varies considerably between the different topologies. The wild-type protein **p1** and the non-cross-linked variants **p2**, **p3**, and **p4** exhibit strong sensitivity toward GuHCl with the absence of a defined melting curve at 1.5 M GuHCl (Figures 2B and S5). Cross-linking increases thermal stability in presence of GuHCl in all three cases (Figures 2C and S5), with the most stable cross-linked trimer **p4$_3$Ta$_2$** retaining a cooperative unfolding profile up to 1.5 M GuHCl.

Given the resistance of the covalently linked trimers to chemical denaturation, we tested if this translates into increased enzymatic activity under these conditions. PFE esterase activity was analyzed by monitoring the conversion of *p*-nitrophenyl acetate to *p*-nitrophenolate (*p*-NP, Figure S6).[38] In the absence of denaturant, all proteins show comparable activity (Figure 2D) indicating that enzyme activity has not been affected by cysteine variation and cross-linking. As expected, all enzymes experience a reduction in activity with increasing concentrations of GuHCl (Figure 2D; Table S7). However, cross-linking considerably enhanced resistance to the denaturant, with highest residual activities observed for bicyclic PFE trimer **p4$_3$Ta$_2$** (Figure 2D). Although unmodified **p1** only facilitates product formation up to 1 M GuHCl (Figure 2E), **p4$_3$Ta$_2$** remains active in the presence of up to 2 M GuHCl (Figure 2F).

Bicyclic p4$_3$Ta$_2$ resists aggregation

Bicyclic trimer **p4$_3$Ta$_2$** experienced the largest stabilizing effect, surpassing both single-cross-linked trimers (**p2$_3$Ta** and **p3$_3$Ta**). To further investigate this

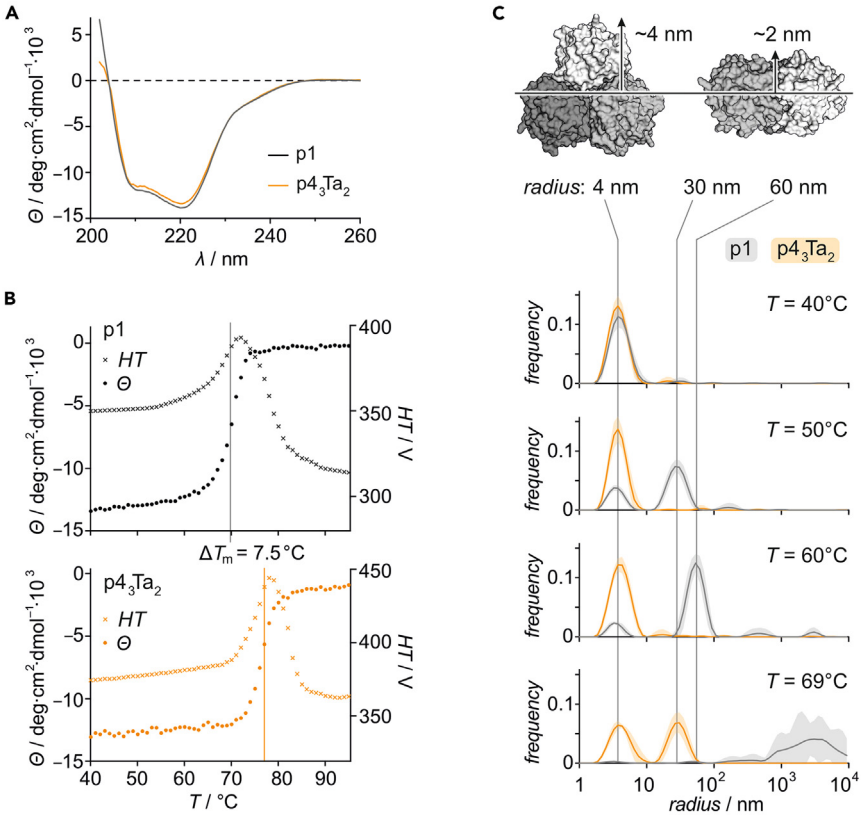

Figure 3. Bicyclic $p4_3Ta_2$ resists aggregation

(A) Circular dichroism (CD) spectra of **p1** and $p4_3Ta_2$ measured at 20°C at a 4 μM trimer concentration (in 50 mM potassium chloride, 50 mM potassium phosphate, pH 8).

(B) Thermal denaturation CD profiles of **p1** (T_m = 69.5°C) and $p4_3Ta_2$ (T_m = 77.0°C) measured at 220 nm. *HT* values suggest precipitation close to the midpoint temperature (T_m derived from the maximum of the CD first derivative curve as presented in Figure S7).

(C) Top: PFE trimer structure (PDB: 1va4) with approximate distances. Bottom: temperature-dependent size distribution derived from DLS experiment for **p1** (gray) and $p4_3Ta_2$ (orange). Measured at a 15 μM trimer concentration (in 50 mM HEPES, 50 mM NaCl, pH 8). The errors account for 1σ (n = 6). Above 69°C, it was not possible to reliably fit size distribution data for **p1**. For $p4_3Ta_2$ data at higher temperatures, see Figure S8.

pronounced stabilization, $p4_3Ta_2$ was studied in more detail. Circular dichroism (CD) spectra under native conditions revealed a spectrum analogous to the wild-type enzyme **p1**, suggesting an unchanged overall fold (Figure 3A). Assessing the thermal denaturation behavior via CD (λ = 220 nm, Figure 3B), melting temperatures were obtained (**p1** T_m = 69.5°C; $p4_3Ta_2$ T_m = 77.0°C), which are in the range of above DSF results (Figure 2A). The slightly higher difference suggested a time dependence of stability, with a slower temperature ramp rate applied for CD compared with DSF measurements. We noted the complete absence of CD signal at high temperature (Figure S7) and the distinctive spike in the associated high tension (*HT*) values (Figure 3B, overlaid), both suggesting that the predominant inactivation pathway involves protein aggregation and subsequent precipitation.[39]

To compare the aggregation behaviors of **p1** and $p4_3Ta_2$, dynamic light scattering (DLS) measurements were performed, confirming for both the presence of homogeneous, well-dispersed trimers at ambient temperatures (up to T = 40°C, Figure 3C). Notably, the observed radius ($r \sim 4$ nm) corresponds to the size of the PFE trimer in

the crystal structure (Figure 3C). For **p1** (gray), temperature-dependent DLS measurements indicated the appearance of higher-order oligomeric structures around 45°C (Figure S8). Initially, species with a radius of ca. 30 nm (T = 50°C) and 60 nm (T = 60°C) were detected. At 69°C, we mainly observed the presence of aggregates >1 μm, which corresponds to the CD-derived melting temperature of **p1** (T_m = 69.5°C). Above 69°C, it was not possible to reliably fit size distribution data for **p1**, most likely due to severe precipitation.

In comparison, bicyclic **p4$_3$Ta$_2$** (orange) remained broadly monodisperse up to 65°C (Figure S8) suggesting a delay of aggregation onset by ca. 20°C. At 69°C, **p4$_3$Ta$_2$** shows species with increased size around 30 nm, analogous to **p1** at 50°C (Figure 3C). Eventually, **p4$_3$Ta$_2$** also showed additional higher-order oligomeric states (60 nm at 70°C and >1 μm at 74°C, Figure S8). To further assess the effect of aggregation on long-term stability, we tested storage at 50°C, a temperature below the melting temperatures of both proteins (**p1** T_m = 69.5°C; **p4$_3$Ta$_2$** T_m = 77.0°C). After 24 h incubation at 50°C, both enzymes retained their activity (Figure S9). After longer storage (more than 1 day), however, **p1** lost activity, whereas **p4$_3$Ta$_2$** kept its activity for multiple weeks. At this temperature, unmodified **p1** already showed the formation of oligomeric structures (Figure 3C), which could lead to aggregation and loss of enzymatic activity over longer time periods.

Crystal structure of bicyclic p4$_3$Ta$_2$

In pursuit of a crystal structure of **p4$_3$Ta$_2$**, conditions were screened to obtain suitable crystals for X-ray diffraction analysis. A dataset was collected, determining the crystal structure of **p4$_3$Ta$_2$** at a resolution of 2.5 Å (PDB: 8pi1, space group C121, Table S8) following molecular replacement with the PFE trimer as a search model (derived from PDB: 1va4). The obtained structure harbors five protomers of **p4$_3$Ta$_2$** per asymmetric unit (Figure 4A). Between both introduced cross-linking sites (C3 and C174) additional well-defined electron density was observed that matches the molecular structure of the cross-link (Figure 4B), thereby validating the expected site-specific modification and bicyclization of the **p4** trimer.

Overall, the crystal structure of **p4$_3$Ta$_2$** (orange) aligns closely with the previously reported structure of wild-type PFE (**p1**, gray, Figure 4C, backbone atom root-mean-square deviation [RMSD]: 0.18 Å), demonstrating minimal perturbation of the macromolecular structure despite the modification of six residues within the cross-linked trimer. On one face of the trimer (top view), the cross-link connects the three N-terminal cysteines (C3) located in a short β strand. On the other side (bottom view), the cross-linked central cysteines (C174) are located at the beginning of an α helix (Figure 4C). Interestingly, at both sites, the cross-link is located within the cavity formed at the junction of the three protein monomers (Figure 4D).

Bicyclization of structurally diverse homotrimeric proteins

The bicyclization of trimeric PFE provides a unique architecture that has not been reported for protein complexes before. To assess the applicability of this approach to other homotrimeric proteins, we searched the RCSB PDB for C3-symmetric homotrimers with 50–400 residues per monomer and identified ca. 4,000 structures. To simplify protein production and characterization, this pool was reduced by selecting for proteins with a hexahistidine tag, at least one tryptophan, and confirmed expression in *E. coli*. In addition, we allowed a maximum of one cysteine residue per monomer to minimize off-target reactivity. These filter criteria produced an initial set of 119 trimers (Table S9), of which 18 structurally diverse protein complexes spanning 14 unique folds, as classified by their class, architecture,

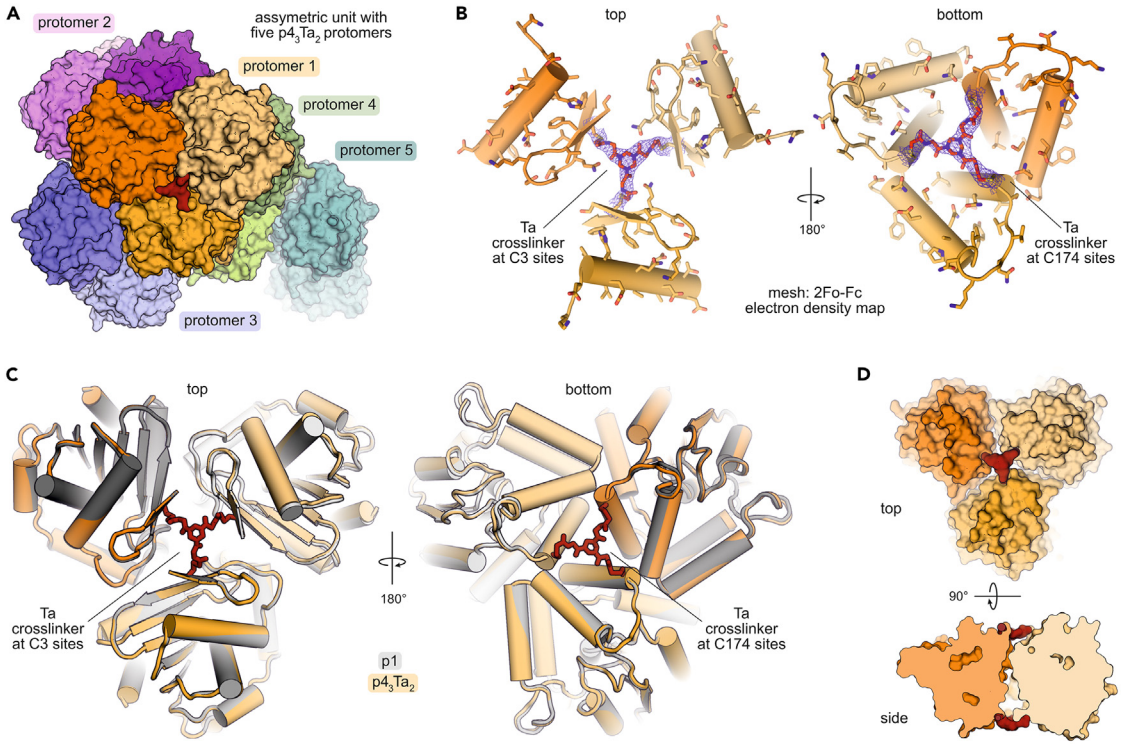

Figure 4. Crystal structure of bicyclic p4$_3$Ta$_2$

(A) The asymmetric unit contains five **p4$_3$Ta$_2$** protomers (space group: C121, for details see Table S8).

(B) 2Fo−Fc electron density map around Ta cross-linked via cysteines C3 and C174, respectively, in the three monomers in **p4$_3$Ta$_2$**.

(C) Overlayed crystal structures of **p1** (gray, PDB: 1va4) and **p4$_3$Ta$_2$** (orange, backbone atom RMSD: 0.18 Å).

(D) Surface representation of **p4$_3$Ta$_2$** showing protein subunits (orange) and Ta cross-links (red).

topology, and homologous superfamily (CATH) domain identities,[40] were selected after visual inspection. To enable bicyclization, two residues per monomer were substituted for cysteine, with distances of 8–15 Å between Cα atoms of the resulting cysteine triplet, producing a total of 18 designs (Tables S10 and S11). Protein variants were expressed in BL21(DE3) cells in an IPTG inducible pET28(+) vector, retaining the purification tags from the original PDB sequences. Expression and purification were successful for 17 of the 18 variants (>0.5 mg protein from 1.5 L culture).

Cross-linking reactions with Ta-I$_3$ were performed in analogy to the bicyclization of **p4**. Initially, stabilization effects were analyzed by thermal denaturation experiments using DSF to compare T_i values prior to and after cross-linking. Of the 17 obtained proteins, 10 showed a substantial increase in thermostability upon Ta-I$_3$ treatment ($\Delta T_i > 5°C$, Figures S10 and S11) with 7 of them surpassing the stabilization effects observed for PFE ($\Delta T_i > 10°C$). The ten proteins that showed clearly increased thermal stability upon cross-linker treatment were analyzed by high-performance liquid chromatography (HPLC) coupled with MS to assess their cross-linking status. For five, we did not obtain interpretable spectra, which may suggest inhomogeneity or incompleteness of the cross-linking reaction or could be a result of the inherent technical difficulties of MS analysis of large, interlinked protein chains. For the remaining five variants, we confirmed covalent trimer formation (Figures S12–S16). One of these, however, only reacted with one cross-linker (Figure S12). For the other four complexes (Figure 5), we confirmed the formation of

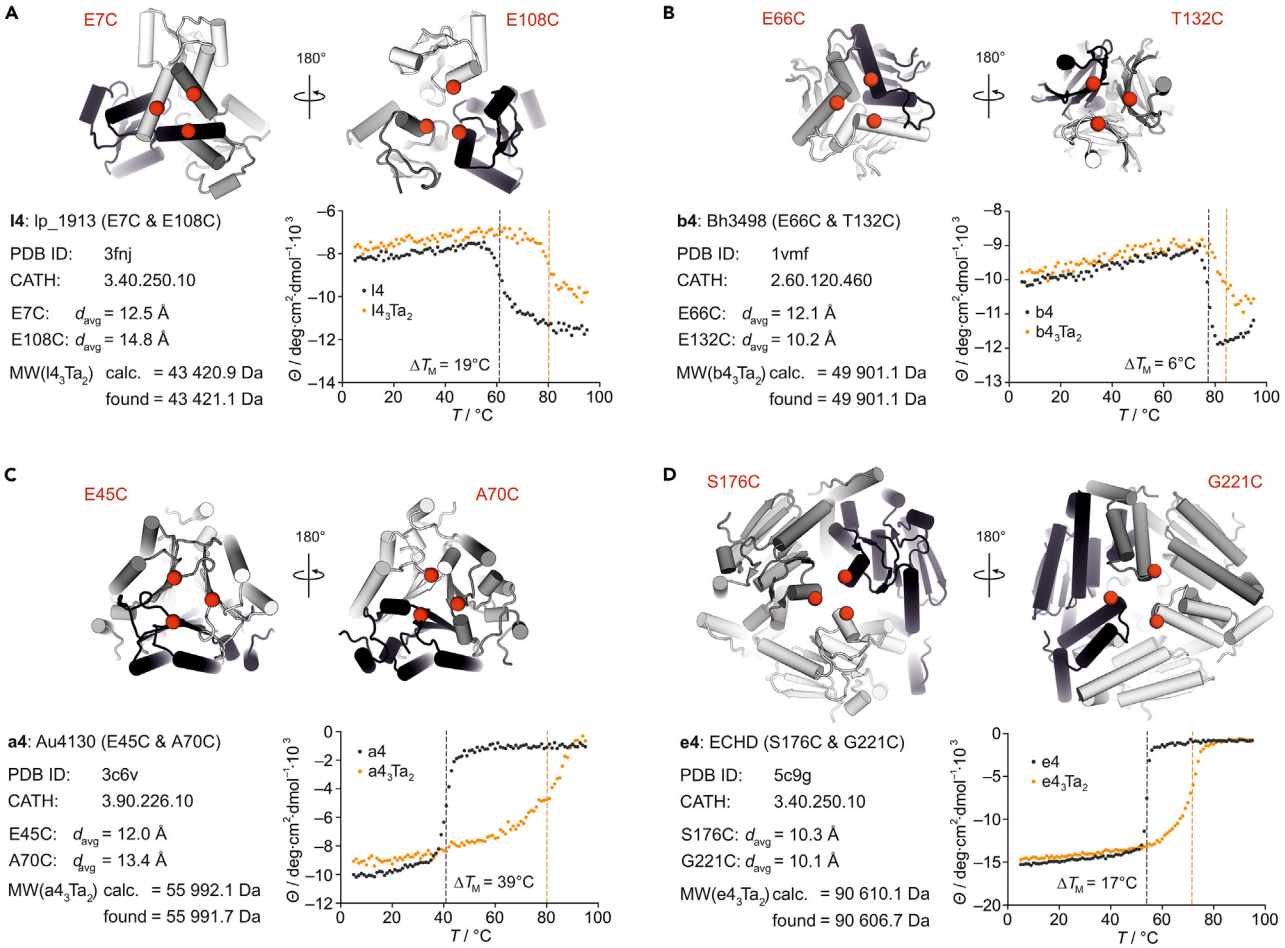

Figure 5. Stabilization of different homotrimeric proteins via bicyclization

(A) Characterization of **l4$_3$Ta$_2$** (lp1913, PDB: 3fnj).

(B) Characterization of **b4$_3$Ta$_2$** (BH3489, PDB: 1vmf).

(C) Characterization of **a4$_3$Ta$_2$** (Au4130, PDB: 3c6v).

(D) Characterization of **e4$_3$Ta$_2$** (ECHD, PDB: 5c9g). Reported crystal structures and cysteine variation sites with average distances (d_{avg}) between Cα atoms of cross-linking residues are shown. Calculated and found molecular weights (MWs) and CD-derived thermal denaturation curves of unmodified (black) and corresponding cross-linked trimers (orange) are provided, including the resulting difference in melting temperatures (ΔT_m). T_m values (Table S12) represent the maximum of the first derivative (corresponding *HT* curves and CD spectra are available in Figure S18).

the bis-crosslinked trimers (monomer$_3$Ta$_2$, Figures S13–S16), additionally validated by SDS-PAGE (Figure S17).

The four confirmed bicyclic proteins originate from a diverse set of structural classes with MWs ranging from 34 to 91 kDa, and distances between introduced cross-linking sites ranging from 10 to 15 Å (Figure 5). To further validate their thermal stability, CD thermal denaturation experiments were performed providing increases in melting temperatures (ΔT_m = 6°C–39°C) in line with DSF-derived values. The smallest bicyclic trimer, **l4$_3$Ta$_2$** (MW = 34 kDa, Figure 5A), was derived from lp_1913,[41] a rhodanese-like domain from *Lactobacillus plantarum*, and revealed a considerably increased melting temperature (ΔT_m = 19°C). Bicyclization of the BH3498[42] variant **b4** resulted in **b4$_3$Ta$_2$** (MW = 50 kDa, Figure 5B) experiencing the smallest stabilization effect (ΔT_m = 6°C) among the four tested variants. The heterologous interfaces of this highly compact trimeric structure are large relative to the size of the trimer, which may explain the moderate stability enhancement upon cross-linking. Thermal denaturation of **l4$_3$Ta$_2$** and **b4$_3$Ta$_2$**, as

well as their monomeric precursors (**l4** and **b4**), produced an unexpected reduction in ellipticity at 220 nm; however, this wavelength remained the most effective way of assaying unfolding by CD. As the third example, bicyclic trimer **a4$_3$Ta$_2$** (Figure 5C) was derived from Au4130,[43] an uncharacterized enzyme from *Aspergillus fumigatus* containing a tautomerase-3 domain. It showed the most pronounced thermo-stabilization effect upon cross-linking (ΔT_m = 39°C). Notably, the un-cross-linked protein itself was the least stable of the tested targets (T_m = 41°C). The fourth bicyclic trimer **e4$_3$Ta$_2$** (Figure 5D), originated from ECHD, a putative enoyl-coenzyme A (coA) hydratase variant,[44] shares the most structural similarity with PFE among the four additional proteins. However, the sequence similarity is minimal (22% sequence identity), and their structural domains are non-homologous. Bicyclization of **e4** again resulted in a substantially increased thermal stability (ΔT_m = 17°C).

Conclusions

We report the bicyclization and stabilization of trimeric proteins, which have been considered particularly difficult targets for stabilization efforts. In the case of PFE, bicyclization enhanced enzyme activity under chemical stress and reduced the formation of higher-order aggregates, as well as precipitation. This suggests that the cross-links tether the quaternary structure, thereby preventing exposure of the hydrophobic interior, which, in turn, results in a reduced tendency to nucleate initial, soluble aggregation states. This may also be supported by the polar nature of the cross-link conveying additional solubility. Most notably, the increased thermal stability and solubility of **p4$_3$Ta$_2$** results in an exceptional longevity with full enzyme activity after more than 3 weeks of storage in buffer at 50°C.

Crucially, we show the bicyclization strategy to be applicable across diverse structural domains. The protein conjugates we present here constitute an abiological topology and were obtained by converting protein complexes into quasi-tertiary structures with augmented connectivity. This topology results in increased compactness in the denatured state and may thereby mimic an intermediate state in the protein folding trajectory. Such systems can therefore shed new light on protein folding and its modulation.[2,45–47] Considering the crucial role of proteins in emergent biotechnological and biomedical applications, the reported chemically modified complexes constitute an attractive modality for applications in sustainable biocatalysis, protein therapy, and diagnostics.

EXPERIMENTAL PROCEDURES

Further experimental procedures can be found in the supplemental information.

Resource availability

Lead contact

Further information and requests for resources should be directed to and will be fulfilled by the lead contact, Tom Grossmann (t.n.grossmann@vu.nl).

Materials availability

All materials generated in this study are available from the lead contact with a completed materials transfer agreement and reasonable compensation by the requestor for its production, processing, and shipping.

Data and code availability

The crystal structure of **p4$_3$Ta$_2$** (bicyclic PFE) has been deposited to the PDB with accession number PDB: 8pi1. All other data supporting this study are available in the manuscript and supplemental information.

Synthesis of Ta-I_3

A round bottom flask was charged with 100 mg (0.206 mmol, 1 equiv) of Ta-Cl_3 (obtained as earlier reported)[27] and suspended in 2.1 mL acetone. Sodium iodine 559 mg (3.70 mmol, 18 equiv) was added, and the reaction mixture was stirred vigorously at room temperature for 16 h. 2 mL of water was added, and the clear yellowish solution was directly subjected to reversed-phase chromatography (water + 0.1% formic acid (FA)/acetonitrile (ACN) + 0.1% FA 90/10 to 10/90 in 15 min). Pure fractions were combined and lyophilized to give 120 mg (0.157 mmol) of a white lyophilizate with 76% yield. ^{1}H NMR (600 MHz, MeOD) δ 5.37 (s, 6H), 4.28 (s, 6H), 3.80 (s, 6H). ^{13}C NMR (151 MHz, MeOD) δ 171.86, 169.79, 56.93, 42.59, -2.45. High-resolution MS (Agilent 6230 ESI-TOF HPLC-MS) calculated for $C_{15}H_{21}I_3N_6O_6Na^+$ $[M + Na]^+$ = 784.8549, found 784.8510.

Cross-linking reactions

Protein cross-linking was carried out by mixing 15 μM of protein (trimer concentration, i.e., monomer concentration of 45 μM) with 1 mM of Ta-Cl_3 or 0.3 mM of Ta-I_3 (freshly prepared in buffer at a concentration of 5 or 1 mM, respectively) in 50 mM HEPES, 50 mM NaCl buffered at pH 8, in a total reaction volume of 80–300 μL. Prior to cross-linking, protein stocks were concentrated to at least 65 μM (trimer concentration) in purification buffer (50 mM HEPES, 150 mM NaCl, at pH 8). This buffer also contained 0.5 mM TCEP to ensure reduction of cysteine side chains prior to cross-linking. The subsequent dilution of the protein upon mixing with the cross-linker resulted in dilution of the TCEP concentration to a maximum of 115 μM. Reactions were incubated at 20°C (except where indicated) overnight (Ta-Cl_3), or 2–4 h (Ta-I_3), and excess cross-linker was subsequently removed by buffer exchange with an Amicon centrifugal concentrator. Cross-linked samples for crystallography were further purified by an additional size exclusion chromatography step, as in the supplemental information section protein expression and purification. Cross-linking reactions for the determination of predominant charge states of PFE variants **p2$_3$Ta**, **p3$_3$Ta**, and **p4$_3$Ta$_2$** were quenched by addition of formic acid to a final concentration of 1% (v/v).

Thermal denaturation (DSF and CD)

Thermal stability was initially assessed by DSF using a Tycho NT.6 instrument. The fluorescence ratio of 350/330 nm was measured between 35°C–95°C (with a temperature ramp rate of 30°C/min) at a protein trimer concentration of 5 μM (50 mM HEPES, 50 mM NaCl, pH 8) and a given concentration of GuHCl. The fixed temperature ramp rate of this instrument is 30°C/min, from which we determined a comparative inflection midpoint (T_i). This value is likely to overestimate absolute stability; therefore, thermal stability was further validated by subsequent CD experiments at reduced ramp rate (1°C/min). Samples for CD were measured at a trimer concentration of 3–5 μM (50 mM potassium phosphate, 50 mM potassium chloride, pH 8) in a 1 mM quartz cuvette in a JASCO J1500 instrument. Thermal melts were recorded at 220 nm from 5°C to 95°C with a ramp rate of 1°C/min to determine the equilibrium unfolding midpoint (T_m). Full spectra were also recorded at 5°C and 95°C between 200 and 260 nm with a bandwidth of 1 nm, averaging four spectra accumulations. *HT* voltage was maintained below 500 V at every wavelength for all measurements. CD measurements are reported as mean residual ellipticity (*MRE*), converted by the following equation, in which n is the number of peptide bonds in the given protein.

$$MRE\left(deg.cm^2.dmol^{-1}\right) = \frac{elipticity\ (mdeg) \times 10^6}{path\ length\ (mm) \times protein\ concentration\ (\mu M) \times n}$$

Relative DSF and CD measurements for unmodified and cross-linked variants were in good accordance (ΔT_i vs. ΔT_m), however absolute T_m values were approximately 5°C–10°C lower, likely due to the slower temperature ramp.

Dynamic light scattering

Temperature-dependent dynamic light scattering (DLS) measurements were obtained using a Prometheus Panta (Nanotemper) instrument at a trimer concentration of 15 μM (50 mM HEPES, 50 mM NaCl, pH 8). Measurements were taken at 0.17°C intervals with a temperature ramp rate of 1°C/min. The determined autocorrelation function at each given temperature was fitted to obtain a size distribution using Panta Control (version 1.6.3) software. Six size distribution fits within a +0.95°C range of the temperature were averaged (e.g., data for T = 50°C represent an average of six measurements between 50.00°C and 50.95°C). The cumulant radii (indicating the predominant particle size) for both samples at every measured temperature between 20°C and 95°C were also calculated using Panta Control software, presented in Figure S8.

Crystallography

Initial screening of crystallization conditions was performed using the JSCG core suite I–IV at 20°C. Screens were assembled in 96-well plates using the sitting-drop vapor diffusion method, with a drop volume of 200 nL dispensed by a Mosquito crystallization robot (SPT Labtech). A protein concentration of 20 mg/mL was mixed in a 1:1 ratio with each crystallization solution. Refinement screens (drop size 1 μL) from initial hits identified two optimal crystallization solutions for growth of $\mathbf{p4_3Ta_2}$ crystals: solution I (100 mM *N*-cyclohexyl-2-aminoethanesulfonic acid, pH 10, 25% [w/v] PEG3000) and crystallization solution II (210 mM lithium acetate, 19% [w/v] PEG3350). Obtained crystals were collected, cryo-protected by soaking in 15%–20% (v/v) glycerol, and flash frozen in liquid nitrogen. Diffraction data were obtained at the i04 beamline at the Diamond Light Source (United Kingdom). Data were integrated using *xds*[48] and two datasets were scaled using *xscale*. The crystal structure was solved by molecular replacement using *Phaser* within the CCP4i2 software suite[49] and PDB: 1va4 as a model. Structure building and refinement was performed using *Coot*, *Refmac5*, and *PDBRedo*. X-ray collection and refinement statistics are provided in Table S8. The crystal structure of bicyclic $\mathbf{p4_3Ta_2}$ has been deposited to the PDB: 8pi1.

SUPPLEMENTAL INFORMATION

Supplemental information can be found online at https://doi.org/10.1016/j.chempr.2023.10.003.

ACKNOWLEDGMENTS

We thank David J. Hamilton for support with compound analytics. We thank the user support team, as well as the beamline staff of I04 at the Diamond Light Source (Oxfordshire, UK) for their support. Funding was provided by the European Research Council ERC proof-of-concept, no. 839088 (T.N.G.) and EU Commission in the framework of the Horizon Europe – EIC Transition Open programme, no. 101057978 (Incircular B.V., S.N.).

AUTHOR CONTRIBUTIONS

S.N., S.H., and T.N.G. conceived and designed the project. P.P. and M.I. performed the chemical synthesis. Protein expression and cross-linking was performed by G.H.H., S.K., P.P., I.D., and S.N. MS characterization data processing was performed

by A.H.L., R.S., and A.M.R. Enzyme activity measurements, as well as DSF and CD analysis, were performed by G.H.H., S.K., and J.O. Protein crystallography and data processing was performed by S.K., N.M.P., and S.H. All authors analyzed the results. All authors discussed the results and commented on the manuscript. G.H.H., S.N., S.H., and T.N.G. prepared the manuscript.

DECLARATION OF INTERESTS

G.H.H., S.K., P.P., I.D., S.N., S.H., and T.N.G. are listed as inventors on a patent application related to the cross-linking of protein complexes. S.N., S.H., and T.N.G. are co-founders and shareholders of Incircular BV, commercializing the corresponding bioconjugation technology. S.H. and T.N.G. are advisers of Incircular BV.

INCLUSION AND DIVERSITY

We support inclusive, diverse, and equitable conduct of research.

Received: July 15, 2023
Revised: September 22, 2023
Accepted: October 6, 2023
Published: November 2, 2023

REFERENCES

1. Bornscheuer, U.T., Huisman, G.W., Kazlauskas, R.J., Lutz, S., Moore, J.C., and Robins, K. (2012). Engineering the third wave of biocatalysis. Nature *485*, 185–194. https://doi.org/10.1038/nature11117.

2. Horne, W.S., and Grossmann, T.N. (2020). Proteomimetics as protein-inspired scaffolds with defined tertiary folding patterns. Nat. Chem. *12*, 331–337. https://doi.org/10.1038/s41557-020-0420-9.

3. Benítez-Mateos, A.I., Roura Padrosa, D., and Paradisi, F. (2022). Multistep enzyme cascades as a route towards green and sustainable pharmaceutical syntheses. Nat. Chem. *14*, 489–499. https://doi.org/10.1038/s41557-022-00931-2.

4. Arnold, F.H. (2018). Directed evolution: bringing new chemistry to life. Angew. Chem. Int. Ed. Engl. *57*, 4143–4148. https://doi.org/10.1002/anie.201708408.

5. Schwizer, F., Okamoto, Y., Heinisch, T., Gu, Y., Pellizzoni, M.M., Lebrun, V., Reuter, R., Köhler, V., Lewis, J.C., and Ward, T.R. (2018). Artificial metalloenzymes: reaction scope and optimization strategies. Chem. Rev. *118*, 142–231. https://doi.org/10.1021/acs.chemrev.7b00014.

6. Hagner, K., Setayeshgar, S., and Lynch, M. (2018). Stochastic protein multimerization, activity, and fitness. Phys. Rev. E *98*. https://doi.org/10.1103/PhysRevE.98.062401.

7. Reetz, M.T. (2013). The importance of additive and non-additive mutational effects in protein engineering. Angew. Chem. Int. Ed. Engl. *52*, 2658–2666. https://doi.org/10.1002/anie.201207842.

8. Magliery, T.J. (2015). Protein stability: computation, sequence statistics, and new experimental methods. Curr. Opin. Struct. Biol. *33*, 161–168. https://doi.org/10.1016/j.sbi.2015.09.002.

9. Chapman, A.M., and McNaughton, B.R. (2016). Scratching the surface: resurfacing proteins to endow new properties and function. Cell Chem. Biol. *23*, 543–553. https://doi.org/10.1016/j.chembiol.2016.04.010.

10. Aalbers, F.S., Fürst, M.J.L.J., Rovida, S., Trajkovic, M., Gómez Castellanos, J.R., Bartsch, S., Vogel, A., Mattevi, A., and Fraaije, M.W. (2020). Approaching boiling point stability of an alcohol dehydrogenase through computationally-guided enzyme engineering. eLife *9*. https://doi.org/10.7554/eLife.54639.

11. Fujita, D., Suzuki, R., Fujii, Y., Yamada, M., Nakama, T., Matsugami, A., Hayashi, F., Weng, J.-K., Yagi-Utsumi, M., and Fujita, M. (2021). Protein stabilization and refolding in a gigantic self-assembled cage. Chem *7*, 2672–2683. https://doi.org/10.1016/j.chempr.2021.08.005.

12. Nooren, I.M.A., and Thornton, J.M. (2003). Diversity of protein-protein interactions. EMBO J. *22*, 3486–3492. https://doi.org/10.1093/emboj/cdg359.

13. Bosshart, A., Panke, S., and Bechtold, M. (2013). Systematic optimization of interface interactions increases the thermostability of a multimeric enzyme. Angew. Chem. Int. Ed. Engl. *52*, 9673–9676. https://doi.org/10.1002/anie.201304141.

14. Meng, Q., Capra, N., Palacio, C.M., Lanfranchi, E., Otzen, M., Van Schie, L.Z., Rozeboom, H.J., Thunnissen, A.W.H., Wijma, H.J., and Janssen, D.B. (2020). Robust ω-transaminases by computational stabilization of the subunit interface. ACS Catal. *10*, 2915–2928. https://doi.org/10.1021/acscatal.9b05223.

15. Kuhlman, B., O'Neill, J.W., Kim, D.E., Zhang, K.Y.J., and Baker, D. (2001). Conversion of monomeric protein L to an obligate dimer by computational protein design. Proc. Natl. Acad. Sci. USA *98*, 10687–10691. https://doi.org/10.1073/pnas.181354398.

16. Robinson, C.R., and Sauer, R.T. (2000). Striking stabilization of Arc repressor by an engineered disulfide bond. Biochemistry *39*, 12494–12502. https://doi.org/10.1021/bi001484e.

17. Li, J.C., Liu, T., Wang, Y., Mehta, A.P., and Schultz, P.G. (2018). Enhancing protein stability with genetically encoded noncanonical amino acids. J. Am. Chem. Soc. *140*, 15997–16000. https://doi.org/10.1021/jacs.8b07157.

18. Liang, H., Sandberg, W.S., and Terwilliger, T.C. (1993). Genetic fusion of subunits of a dimeric protein substantially enhances its stability and rate of folding. Proc. Natl. Acad. Sci. USA *90*, 7010–7014. https://doi.org/10.1073/pnas.90.15.7010.

19. Akanuma, S., Matsuba, T., Ueno, E., Umeda, N., and Yamagishi, A. (2010). Mimicking the evolution of a thermally stable monomeric four-helix bundle by fusion of four identical single-helix peptides. J. Biochem. *147*, 371–379. https://doi.org/10.1093/jb/mvp179.

20. Dellarole, M., Sánchez, I.E., Freire, E., and De Prat-Gay, G. (2007). Increased stability and DNA site discrimination of "single chain" variants of the dimeric β-barrel DNA binding domain of the human papillomavirus e2 transcriptional regulator. Biochemistry *46*, 12441–12450. https://doi.org/10.1021/bi701104q.

21. Hashimoto, K., and Panchenko, A.R. (2010). Mechanisms of protein oligomerization, the critical role of insertions and deletions in maintaining different oligomeric states. Proc. Natl. Acad. Sci. USA *107*, 20352–20357. https://doi.org/10.1073/pnas.1012999107.

22. Schneider, A.F.L., Kithil, M., Cardoso, M.C., Lehmann, M., and Hackenberger, C.P.R. (2021).

Cellular uptake of large biomolecules enabled by cell-surface-reactive cell-penetrating peptide additives. Nat. Chem. *13*, 530–539. https://doi.org/10.1038/s41557-021-00661-x.

23. Kale, S.S., Bergeron-Brlek, M., Wu, Y., Kumar, M.G., Pham, M.V., Bortoli, J., Vesin, J., Kong, X.D., Machado, J.F., Deyle, K., et al. (2019). Thiol-to-amine cyclization reaction enables screening of large libraries of macrocyclic compounds and the generation of sub-kilodalton ligands. Sci. Adv. *5*, eaaw2851. https://doi.org/10.1126/sciadv.aaw2851.

24. Prescher, J.A., Dube, D.H., and Bertozzi, C.R. (2004). Chemical remodelling of cell surfaces in living animals. Nature *430*, 873–877. https://doi.org/10.1038/nature02791.

25. Moore, E.J., Zorine, D., Hansen, W.A., Khare, S.D., and Fasan, R. (2017). Enzyme stabilization via computationally guided protein stapling. Proc. Natl. Acad. Sci. USA *114*, 12472–12477. https://doi.org/10.1073/pnas.1708907114.

26. Pelay-Gimeno, M., Bange, T., Hennig, S., and Grossmann, T.N. (2018). In situ cyclization of native proteins: structure-based design of a bicyclic enzyme. Angew. Chem. Int. Ed. Engl. *57*, 11164–11170. https://doi.org/10.1002/anie.201804506.

27. Neubacher, S., Saya, J.M., Amore, A., and Grossmann, T.N. (2020). In situ cyclization of proteins (INCYPRO): cross-link derivatization modulates protein stability. J. Org. Chem. *85*, 1476–1483. https://doi.org/10.1021/acs.joc.9b02490.

28. Cigler, M., Müller, T.G., Horn-Ghetko, D., von Wrisberg, M.K., Fottner, M., Goody, R.S., Itzen, A., Müller, M.P., and Lang, K. (2017). Proximity-triggered covalent stabilization of low-affinity protein complexes in vitro and in vivo. Angew. Chem. Int. Ed. Engl. *56*, 15737–15741. https://doi.org/10.1002/anie.201706927.

29. Zhou, L., Chai, F., He, Y., Zhou, Z., Guo, S., Li, P., Sun, Q., Zu, X., Liu, X., Huang, Q., et al. (2022). Homodimerized cytoplasmic domain of PD-L1 regulates its complex glycosylation in living cells. Commun. Biol. *5*, 887. https://doi.org/10.1038/s42003-022-03845-4.

30. Nguyen, T.A., Gronauer, T.F., Nast-Kolb, T., Sieber, S.A., and Lang, K. (2022). Substrate profiling of mitochondrial caseinolytic protease P via a site-specific photocrosslinking approach. Angew. Chem. Int. Ed. Engl. *61*, e202111085. https://doi.org/10.1002/anie.202111085.

31. Kiehstaller, S., Hutchins, G.H., Amore, A., Gerber, A., Ibrahim, M., Hennig, S., Neubacher, S., and Grossmann, T.N. (2023). Bicyclic engineered sortase A performs transpeptidation under denaturing conditions. Bioconjug. Chem. *34*, 1114–1121. https://doi.org/10.1021/acs.bioconjchem.3c00151.

32. Timmerman, P., Beld, J., Puijk, W.C., and Meloen, R.H. (2005). Rapid and quantitative cyclization of multiple peptide loops onto synthetic scaffolds for structural mimicry of protein surfaces. Chembiochem *6*, 821–824. https://doi.org/10.1002/cbic.200400374.

33. Heinis, C., Rutherford, T., Freund, S., and Winter, G. (2009). Phage-encoded combinatorial chemical libraries based on bicyclic peptides. Nat. Chem. Biol. *5*, 502–507. https://doi.org/10.1038/nchembio.184.

34. Chen, S., Bertoldo, D., Angelini, A., Pojer, F., and Heinis, C. (2014). Peptide ligands stabilized by small molecules. Angew. Chem. Int. Ed. Engl. *53*, 1602–1606. https://doi.org/10.1002/anie.201309459.

35. Yin, D.L., Bernhardt, P., Morley, K.L., Jiang, Y., Cheeseman, J.D., Purpero, V., Schrag, J.D., and Kazlauskas, R.J. (2010). Switching catalysis from hydrolysis to perhydrolysis in pseudomonas fluorescens esterase. Biochemistry *49*, 1931–1942. https://doi.org/10.1021/bi9021268.

36. Schmidt, M., Hasenpusch, D., Kähler, M., Kirchner, U., Wiggenhorn, K., Langel, W., and Bornscheuer, U.T. (2006). Directed evolution of an esterase from Pseudomonas fluorescens yields a mutant with excellent enantioselectivity and activity for the kinetic resolution of a chiral building block. Chembiochem *7*, 805–809. https://doi.org/10.1002/cbic.200500546.

37. Cheeseman, J.D., Tocilj, A., Park, S., Schrag, J.D., and Kazlauskas, R.J. (2004). Structure of an aryl esterase from Pseudomonas fluorescens. Acta Crystallogr. D Biol. Crystallogr. *60*, 1237–1243. https://doi.org/10.1107/S0907444904010522.

38. Drienovská, I., Gajdoš, M., Kindler, A., Takhtehchian, M., Darnhofer, B., Birner-Gruenberger, R., Dörr, M., Bornscheuer, U.T., and Kourist, R. (2020). Folding assessment of incorporation of noncanonical amino acids facilitates expansion of functional-group diversity for enzyme engineering. Chemistry *26*, 12338–12342. https://doi.org/10.1002/chem.202002077.

39. Muraoka, T., Sadhukhan, N., Ui, M., Kawasaki, S., Hazemi, E., Adachi, K., and Kinbara, K. (2014). Thermal-aggregation suppression of proteins by a structured PEG analogue: importance of denaturation temperature for effective aggregation suppression. Biochem. Eng. J. *86*, 41–48. https://doi.org/10.1016/j.bej.2014.03.001.

40. Knudsen, M., and Wiuf, C. (2010). The CATH database. Hum. Genomics *4*, 207–212. https://doi.org/10.1186/1479-7364-4-3-207.

41. Seetharaman, J., Chen, Y., Forouhar, F., Sahdev, S., Janjua, H., Xiao, R., Ciccosanti, C., Foote, E.L., Acton, T.B., Rost, B., et al. (2008). Crystal structure of the full-length lp_1913 protein from Lactobacillus plantarum, Northeast Structural Genomics Consortium Target LpR140. https://doi.org/10.2210/pdb3FNJ/pdb.

42. Joint Center for Structural Genomics (JCSG) (2004). Crystal structure of a YBJQ-like fold protein of unknown function (BH3498) from Bacillus halodurans at 1.46 A resolution. https://doi.org/10.2210/pdb1VMF/pdb.

43. Singer, A.U., Binkowski, T.A., Skarina, T., Kagan, O., Edwards, A.M., Joachimiak, A., and Savchenko, A.; Midwest Center for Structural Genomics (MCSG) (2008). Crystal structure of AU4130/APC7354, a probable enzyme from the thermophilic fungus Aspergillus fumigatus. https://doi.org/10.2210/pdb3C6V/pdb.

44. Szlachta, K., Cooper, D.R., Chapman, H.C., Cymbrowski, M.T., Stead, M., Hillerich, B.S., Ahmed, M., Bonanno, J., Seidel, R., Almo, S.C., et al. (2015). Crystal structure of a putative enoyl-CoA hydratase/isomerase family protein from Hyphomonas neptunium. https://doi.org/10.2210/pdb5C9G/pdb.

45. Jiang, Y., Neti, S.S., Sitarik, I., Pradhan, P., To, P., Xia, Y., Fried, S.D., Booker, S.J., and O'Brien, E.P. (2023). How synonymous mutations alter enzyme structure and function over long timescales. Nat. Chem. *15*, 308–318. https://doi.org/10.1038/s41557-022-01091-z.

46. Newberry, R.W., and Raines, R.T. (2019). Secondary forces in protein folding. ACS Chem. Biol. *14*, 1677–1686. https://doi.org/10.1021/acschembio.9b00339.

47. Gan, Q., Ferrand, Y., Bao, C., Kauffmann, B., Grélard, A., Jiang, H., and Huc, I. (2011). Helix-rod host-guest complexes with shuttling rates much faster than disassembly. Science *331*, 1172–1175. https://doi.org/10.1126/science.1200143.

48. Kabsch, W. (2010). XDS. Acta Crystallogr. D Biol. Crystallogr. *66*, 125–132. https://doi.org/10.1107/S0907444909047337.

49. Potterton, L., Agirre, J., Ballard, C., Cowtan, K., Dodson, E., Evans, P.R., Jenkins, H.T., Keegan, R., Krissinel, E., Stevenson, K., et al. (2018). CCP4i2: the new graphical user interface to the CCP4 program suite. Acta Crystallogr. D Struct. Biol. *74*, 68–84. https://doi.org/10.1107/S2059798317016035.

Chem, Volume *10*

Supplemental information

Covalent bicyclization of protein complexes yields durable quaternary structures

George H. Hutchins, Sebastian Kiehstaller, Pascal Poc, Abigail H. Lewis, Jisun Oh, Raya Sadighi, Nicholas M. Pearce, Mohamed Ibrahim, Ivana Drienovská, Anouk M. Rijs, Saskia Neubacher, Sven Hennig, and Tom N. Grossmann

Supplementary Experimental Procedures

Molecular Biology

Wild-type PFE (**p1**) in a previously reported construct [1] with a C-terminal His-tag was used to prepare variants **p2**, **p3** and **p4** containing T3C and Q174C mutations by site-directed mutagenesis, via a modified QuikChange (Agilent) protocol as described previously [2], using *Pfu* Turbo polymerase and 27-mer overlapping primers (obtained from IDT). Residual template DNA in the completed PCR reactions was digested by addition of DpnI (NEB) at 37°C for 1 hour followed by transformation of 1–5 µL of the reaction into chemically competent *E. coli* DH5-α cells, mini-prep scale DNA purification and confirmation of successful mutagenesis by Sanger sequencing (Eurofins Genomics).

All other trimeric protein variants (Table S11) were synthesized and cloned by Twist Bioscience in a pET28a (+) expression vector (kanamycin resistant, IPTG inducible). Constructs for the suite of protein trimers were designed to match the exact expressed sequence of proteins deposited to the protein databank, containing either an N-terminal or C-terminal hexa-histidine tag and any additional cleavage sites and tags. Full-length sequences of all expressed proteins are included in Supplementary Figure S1 and Table S11.

Protein Expression and Purification

Protein expression vectors were transformed into *E. coli* BL21(DE3) cells by addition of 10–50 ng of purified plasmid DNA and heat-shock at 42°C for 45 seconds. Transformed colonies were inoculated in 100 mL of LB (with 100 mg/L ampicillin or 50 mg/L kanamycin dependent on resistance) and incubated overnight at 37°C, 130 RPM. 20 mL of overnight culture was transferred to 1 L volumes of LB (containing respective antibiotics) and cultured to an OD_{600nm} of 0.6–0.8 prior to induction by addition of 0.2% (m/v) *L*-rhamnose or 1 mM IPTG and expressed for 16–18 hours at 28°C, 130 RPM. Alternative trimers were expressed as above (50 mg/L kanamycin, 1 mM IPTG) in TB media. Cell pellets were harvested by centrifugation (4000 RPM, 20 minutes) and resuspended in lysis buffer (50 mM Tris, 300 mM NaCl, 20 mM imidazole, pH 8).

Cells were lysed by four passes through a microfluidizer (Microfluidics LM20), and cell debris removed by centrifugation at 18 000 RPM for 30 minutes at 4°C. His-tagged proteins were purified by nickel affinity chromatography, flowing the clarified lysate through a 1 mL HisTrap FF column (Cytiva) equilibrated with lysis buffer at 3 mL/min., followed by further column washing with lysis buffer, and protein elution by increasing imidazole concentration to 250 mM. Protein samples were further purified by size exclusion chromatography with a 16/600 Superdex 75 or 200 pg column (Cytiva), buffered in 50 mM HEPES, 150 mM NaCl, at pH 8. Tris (2-carboxyethyl) phosphine (TCEP) at a concentration of 0.5 mM was added to the size exclusion buffer for purification of crosslinking variants to ensure reduction of exogenous solvent exposed cysteine residues. Successful purification of protein samples was confirmed by SDS-PAGE and LC-MS analysis, and samples were concentrated to 65–150 µM (Amicon centrifugal filtration) and flash frozen in liquid nitrogen for storage at –80°C prior to use. Extinction coefficients (ε) used to determine protein concentration were predicted using the Expasy ProtParam tool [3]. All protein concentrations are reported as *trimeric* concentration, regardless of crosslinking status (*e.g.*, PFE monomeric ε = 36 743 $M^{-1}cm^{-1}$, trimeric ε = 110 229 $M^{-1}cm^{-1}$) unless otherwise stated.

SDS-PAGE

SDS-PAGE samples were prepared by mixing a concentration of 5–20 µM protein with standard Coomassie loading dye and incubated at 95°C for 15 minutes, except (as noted in Figure S17) where a final concentration of 6 M urea was added in addition to loading dye, with no heating. Samples were analysed by a 4–20% gradient gel (GenScript) for 1 hour at 150 V and stained by Instant Blue Coomassie (Abcam).

Protein Liquid Chromatography/Mass Spectrometry

The molecular weight of variants and their crosslinked counterparts was assessed by LC/MS on different systems, indicated for each data collection in the respective supplementary figure. High-resolution MS of PFE variants and their crosslinked counterparts (Table S1) was performed using an UltiMate 3000 RSLCnano system (Thermo Fisher Scientific). The samples were injected on a 1.0 mm I.D. x 30 cm, 4 µM

TSKgel superSW3000 SEC column (Tosoh). The mobile phase comprised of 150 mM ammonium acetate (AA). The isocratic gradient applied was as follows: 0–16 min, 100% AA at a flow rate of 16 μL/min. The injection volume and column temperature were set at 1 μL and 23°C, respectively. This LC set up was coupled to a TIMS-Qq-TOF mass spectrometer (first generation, Bruker equipped with an electrospray-ionization (ESI) source [4]. All measurements were acquired for 16 min operating the mass spectrometer in positive mode with the following ESI and MS settings: capillary voltage of 4.2 kV, nebulizer gas of 0.8 bar, dry gas flow of 4.0 L/min, drying temperature of 200°C, ion energy of 5 eV, collision energy of 10 eV, and in-source collision-induced dissociation at 80 eV. The mass spectrometer was in TIMS-off mode (no ion mobility) using a m/z range of 500–8000. Ion funnels were set at values of 350 Vpp and 600 Vpp. Data analysis was performed using Bruker Compass DataAnalysis. Samples were calibrated externally using Agilent ESI tuning mix for ESI-ToF.

Analysis of PFE variant charge states (Figure 1C) was measured on an Agilent 6230 ESI-TOF LC/MS (3500 V capillary voltage), whilst molecular weight of all other trimeric variants (Figures S12-S16) was determined using either an Agilent 6230 ESI-TOF or LC/MSD XT ESI-Quadrupole LC/MS (3000 V capillary voltage). Both systems were used with the same two LC mobile phases; A (H_2O, 0.1% v/v formic acid) and B (80% isopropanol, 10% acetonitrile, 10% H_2O, 0.1% formic acid v/v), with injection of 0.01-0.1 nmol of protein sample via a 50 x 2.1 mm Agilent AdvanceBio RP mAB reverse-phase C4 column. A 10-minute gradient of 0–95% solvent B was applied with a flow rate of 0.3 mL/min. Mass spectra were recorded in the m/z 500–3000 range at a scan rate of 1.0 Hz. Deconvoluted masses were obtained using the maximum entropy algorithm in Agilent software with a mass range of 10,000–100,000 Da and H^+ as the amplifier. Tables for all LC/MS measurements with the calculated (m/z = [MW+Z]/Z) and found values for all predominant peaks are included in the Supplementary Information.

The calculated molecular weight of each protein trimer was derived from the Expasy ProtParam molecular weight [3], excluding the N-terminal methionine residue which is typically cleaved from expressed protein sequence [5]. An additional mass of approximately +178 Da was frequently observed for both unreacted and crosslinked proteins, corresponding to a previously reported N-linked gluconylation [6]. Crosslinked trimer molecular weights were calculated by addition of the mass of reacted Ta-I_3 (381.4 g/mol), minus the mass of three hydrogens per crosslinker (displaced from the reacted cysteine thiol groups).

PFE Activity Assays

Enzymatic activity was assessed by measuring turnover of *p*-nitrophenyl acetate (*p*NPA) to *p*-nitrophenolate (*p*NP). Guanidine hydrochloride dependent activity was determined by incubating PFE variants at a concentration of 50 nM with GuHCl (0, 0.5, 1, 1.5 and 2 M) for 10 minutes prior to the assay. The substrate stock (*p*NPA) was prepared daily in buffer (50 mM HEPES, 50 mM NaCl, pH 7.5) with 10% DMSO v/v at a concentration of 2 mM. Activity was measured at 20°C at a final trimeric concentration of 2 nM PFE in a 100 μL volume (5% DMSO v/v), in a half-area 96 well microplate, initiating the reaction by addition of a final substrate concentration of 1 mM *p*NPA. Absorbance at 410 nm was measured in a plate reader (TECAN Spark 20M) for up to 30 minutes at an interval of 20 seconds, with shaking at 270 RPM between measurements. An additional measurement without enzyme was taken to determine background hydrolysis of the substrate at a given concentration of GuHCl and subtracted from the data. All assays were carried out in 50 mM HEPES, 50 mM NaCl, at pH 7.5. Long term high temperature storage experiments (Figure S9) were performed using a final trimer assay concentration of 0.67 nM, after incubating the protein at 50°C at a concentration of 30 μM in 50 mM HEPES, 50 mM NaCl, pH 8.

Supplementary Figures

p1 (*PFE wild type*)
MSTFVAKDGTQIYFKDWGSGKPVLFSHGWLLDADMWEYQMEYLSSRGYRTIAFDRRGFGRSDQPWTGNDYDTFA
DDIAQLIEHLDLKEVTLVGFSMGGGDVARYIARHGSARVAGLVLLGAVTPLFGQKPDYPQGVPLDVFARFKTEL
LKDRAQFISDFNAPFYGINKGQVVSQGVQTQTLQIALLASLKATVDCVTAFAETDFRPDMAKIDVPTLVIHGDG
DQIVPFETTGKVAAELIKGAELKVYKDAPHGFAVTHAQQLNEDLLAFLKRGSHHHHHH

p2 (PFE T3C)
MS**C**FVAKDGTQIYFKDWGSGKPVLFSHGWLLDADMWEYQMEYLSSRGYRTIAFDRRGFGRSDQPWTGNDYDTFA
DDIAQLIEHLDLKEVTLVGFSMGGGDVARYIARHGSARVAGLVLLGAVTPLFGQKPDYPQGVPLDVFARFKTEL
LKDRAQFISDFNAPFYGINKGQVVSQGVQTQTLQIALLASLKATVDCVTAFAETDFRPDMAKIDVPTLVIHGDG
DQIVPFETTGKVAAELIKGAELKVYKDAPHGFAVTHAQQLNEDLLAFLKRGSHHHHHH

p3 (PFE Q174C)
MSTFVAKDGTQIYFKDWGSGKPVLFSHGWLLDADMWEYQMEYLSSRGYRTIAFDRRGFGRSDQPWTGNDYDTFA
DDIAQLIEHLDLKEVTLVGFSMGGGDVARYIARHGSARVAGLVLLGAVTPLFGQKPDYPQGVPLDVFARFKTEL
LKDRAQFISDFNAPFYGINKGQVVS**C**GVQTQTLQIALLASLKATVDCVTAFAETDFRPDMAKIDVPTLVIHGDG
DQIVPFETTGKVAAELIKGAELKVYKDAPHGFAVTHAQQLNEDLLAFLKRGSHHHHHH

p4 (PFE T3C+Q174C)
MS**C**FVAKDGTQIYFKDWGSGKPVLFSHGWLLDADMWEYQMEYLSSRGYRTIAFDRRGFGRSDQPWTGNDYDTFA
DDIAQLIEHLDLKEVTLVGFSMGGGDVARYIARHGSARVAGLVLLGAVTPLFGQKPDYPQGVPLDVFARFKTEL
LKDRAQFISDFNAPFYGINKGQVVS**C**GVQTQTLQIALLASLKATVDCVTAFAETDFRPDMAKIDVPTLVIHGDG
DQIVPFETTGKVAAELIKGAELKVYKDAPHGFAVTHAQQLNEDLLAFLKRGSHHHHHH

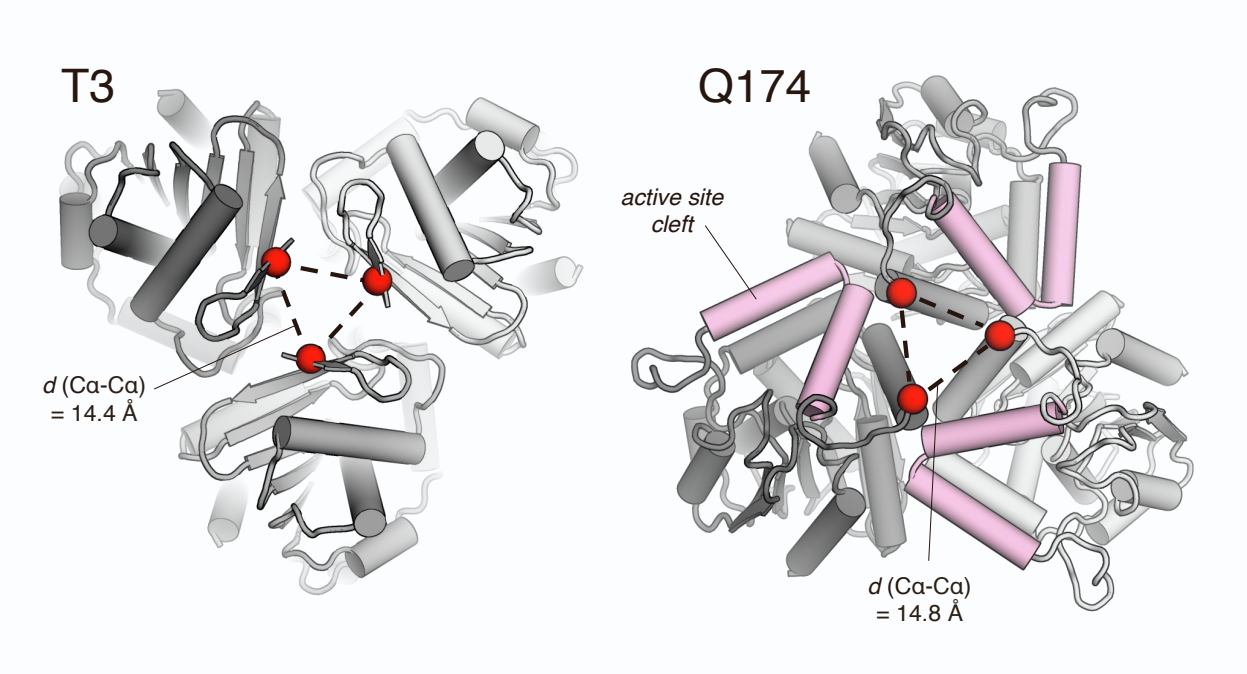

Figure S1. Design schema for PFE trimeric crosslinking (relating to Figure 1A). Top: Expressed sequences of PFE wild type (**p1**) and the three variants designed for trimer crosslinking (**p2**, **p3**, **p4**). Bottom: Dashed lines indicate the distance (*d*) between the C*α* atoms (red) of selected crosslinking sites. Substrate entry to the enzyme active site is via a V-shaped helical hairpin (pink, PDB ID: 1va4).

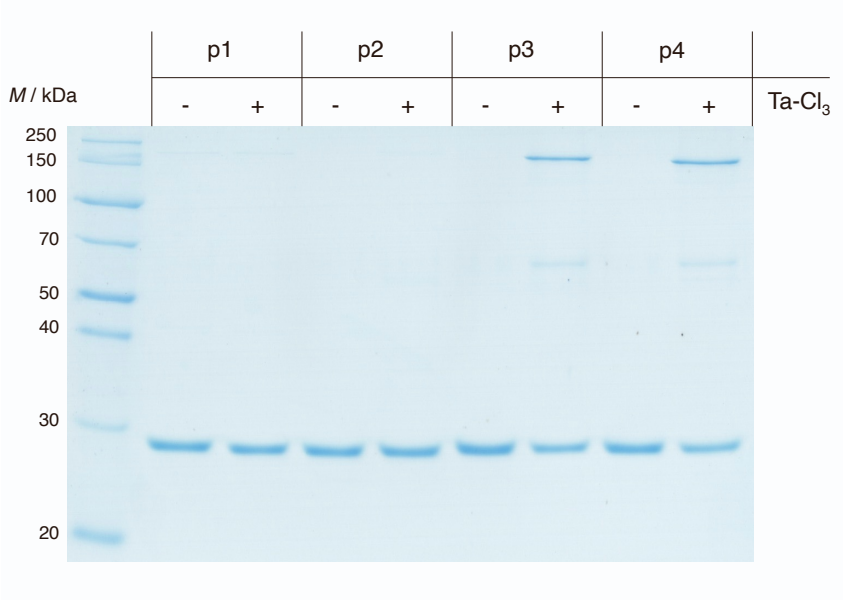

Figure S2. **Reactivity of PFE variants with Ta-Cl_3 (chemical structure in Figure 1B).** Reaction time was 4 hours at 21°C, 15 µM protein trimer, 300 µM Ta-Cl_3. No reactivity is observed with **p2** (T3C) whilst limited reactivity is observed with **p3** (Q174C) and **p4** (T3C + Q174C) resulting in partial formation of covalently linked trimers (top band) and a small proportion of dimer (middle band).

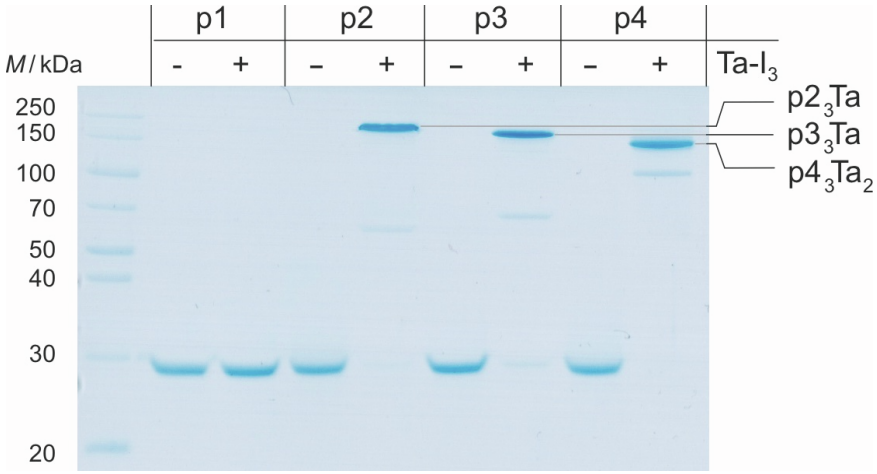

Figure S3. **Reactivity of PFE variants with Ta-I_3 (chemical structure in Figure 1B).** SDS-PAGE analysis of PFE variants prior and after incubation with Ta-I_3 demonstrates the formation of covalently linked, higher molecular weight species, and hinted at the modified chain topology with variable band migration (**p4$_3$Ta$_2$** > **p3$_3$Ta** > **p2$_3$Ta**) despite equivalent molecular weight.

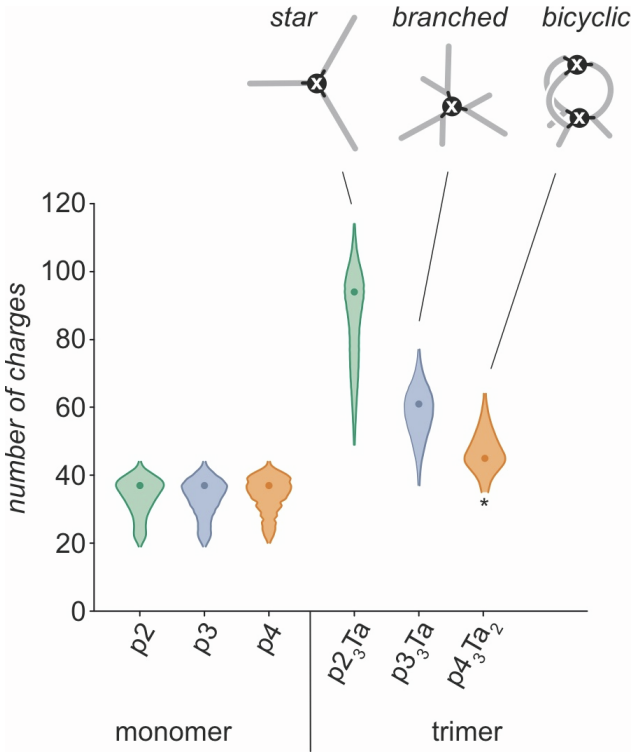

Figure S4. Violin plot showing distribution and range of charge states for PFE variants p2–p4 and crosslinked variants p2–p4 as observed by TOF-LC/MS, relating to Figure 1C. For MS signals and intensities see Tables S2–S5. *Due to the m/z range of the instrument lower charge states could not be detected. Raw data for **p2$_3$Ta**, **p3$_3$Ta** and **p4$_3$Ta$_2$** are presented in Figure 1C.

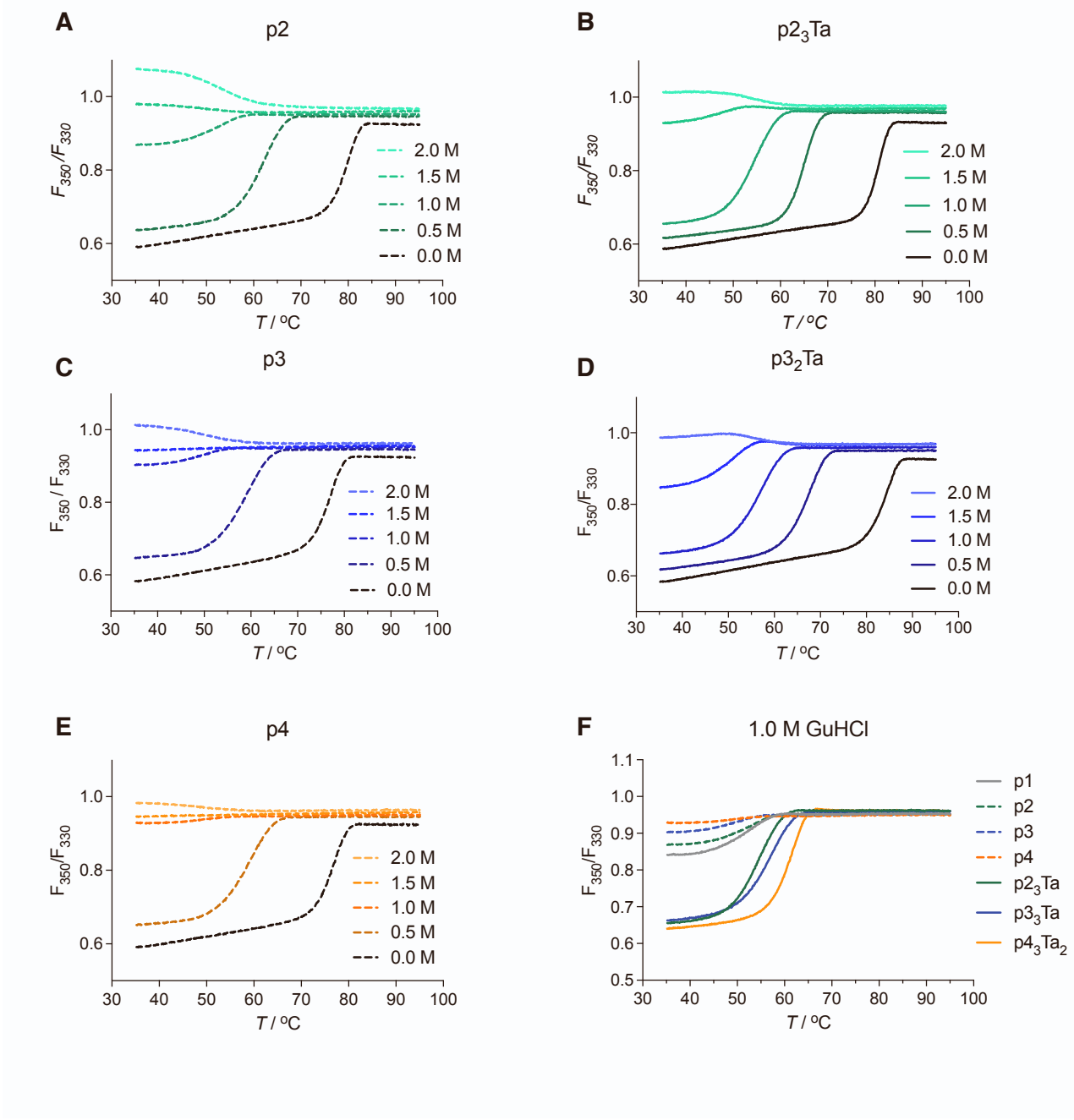

Figure S5. Thermal melt curves for PFE variants and their crosslinked counterparts. (A–E) Additional thermal denaturation curves (DSF measurements of tryptophan fluorescence ratio) for PFE variants **p2**–**p4** before and after crosslinking by Ta-I_3. Midpoint inflection temperatures (T_i) are reported in Figure 2A and Table S6. (F) Comparison of thermal denaturation curves for all variants at 1 M GuHCl further demonstrates the resistance of crosslinked PFE to chemical stress, an effect which is most pronounced for bicyclic **p4$_3$Ta$_2$**.

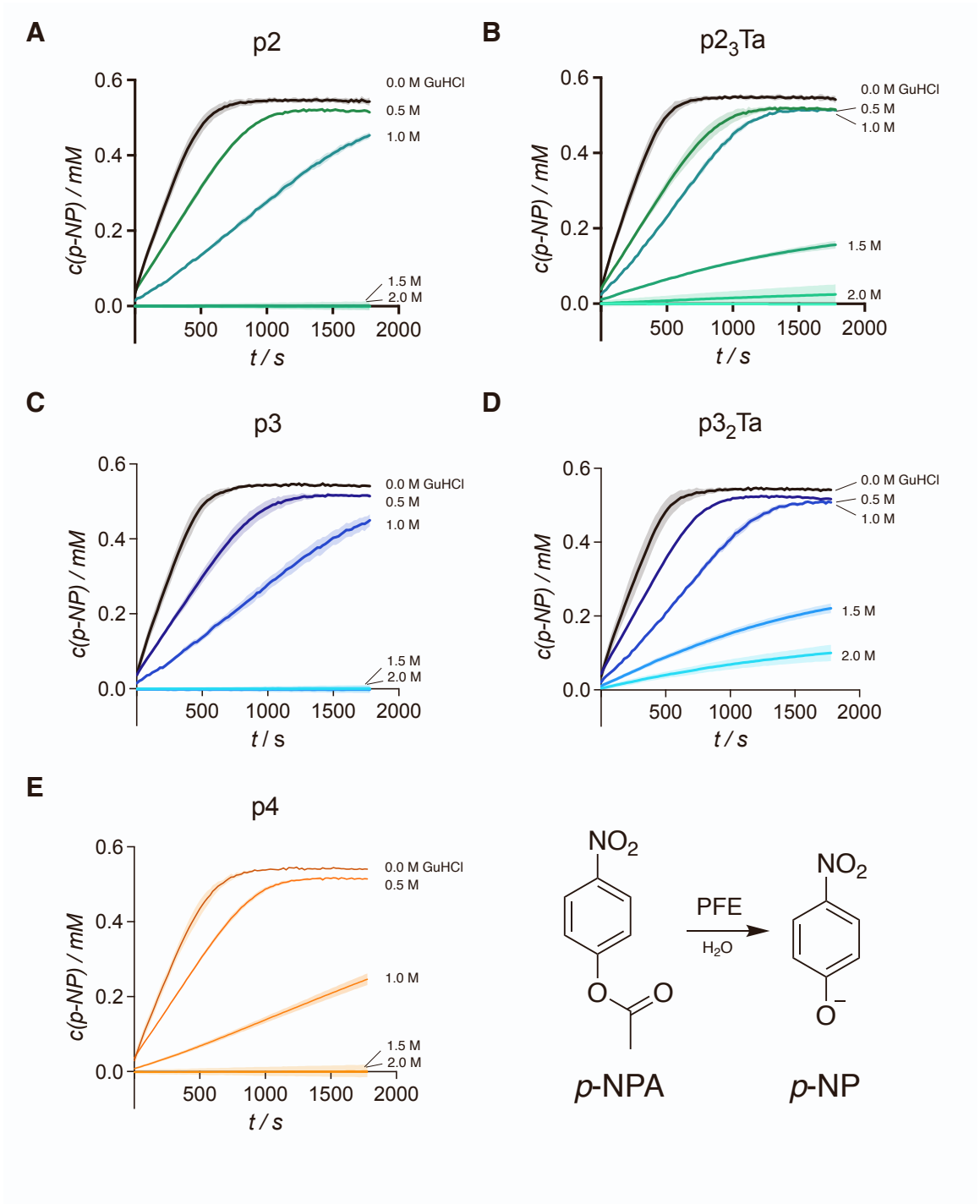

Figure S6. Enzymatic activity for PFE variants and their crosslinked counterparts. Activity assayed by hydrolysis of *para*-nitrophenyl acetate (*p*-NPA) to *para*-nitrophenolate (*p*-NP). Additional assay data shown for PFE variants **p2**–**p4** before and after crosslinking. The initial reaction rate relative to that of **p4$_3$Ta$_2$** for each concentration of GuHCl was used to compare variants reported in Figure 2D (for absolute values with errors see Table S7). Triplicate technical repeats, standard error shaded.

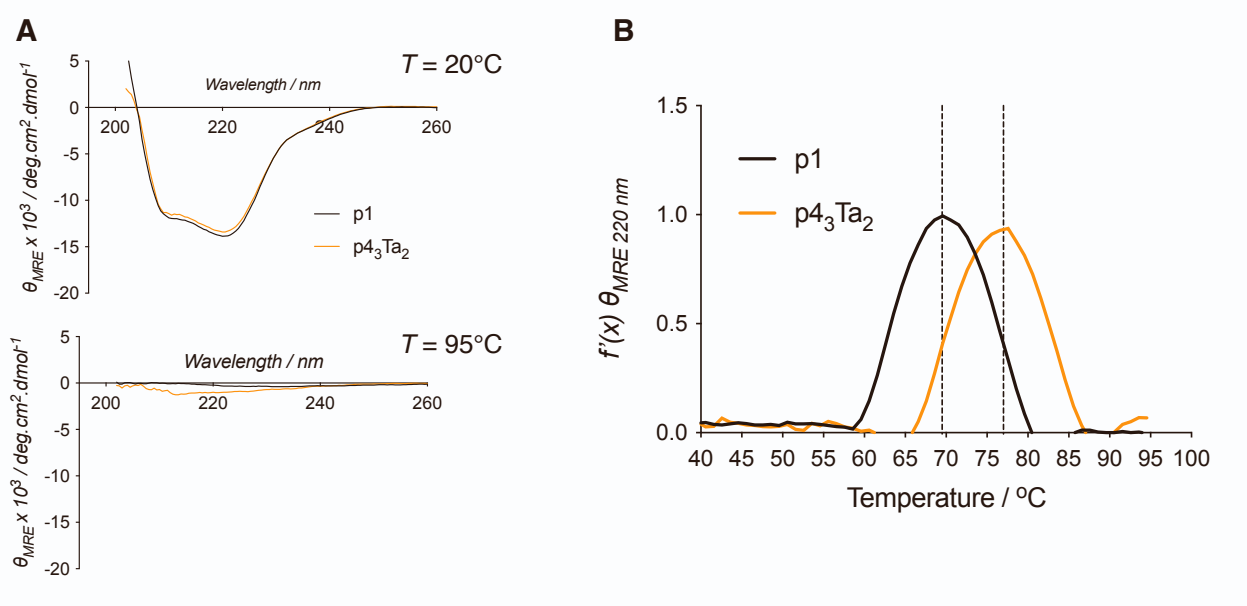

Figure S7. Circular dichroism spectroscopy of PFE variants (relates to Figures 3A and 3B). (A) Circular dichroism spectra of PFE variants **p1** and **p4$_3$Ta$_2$** at 20°C (also shown in Figure 3A) and 95°C at a 4 μM trimer concentration (in 50 mM potassium chloride, 50 mM potassium phosphate, pH 8). At 20°C, we obtained equivalent CD spectra for both **p1** and **p4$_3$Ta$_2$**, showing characteristic two minima around 210 and 220 nm corresponding to the predominantly helical fold of the trimer. The absence of signal at 95°C suggests complete precipitation of the protein. (B) First derivative of melt curves, T_m values (Figure 3B) were determined at the curve maximum.

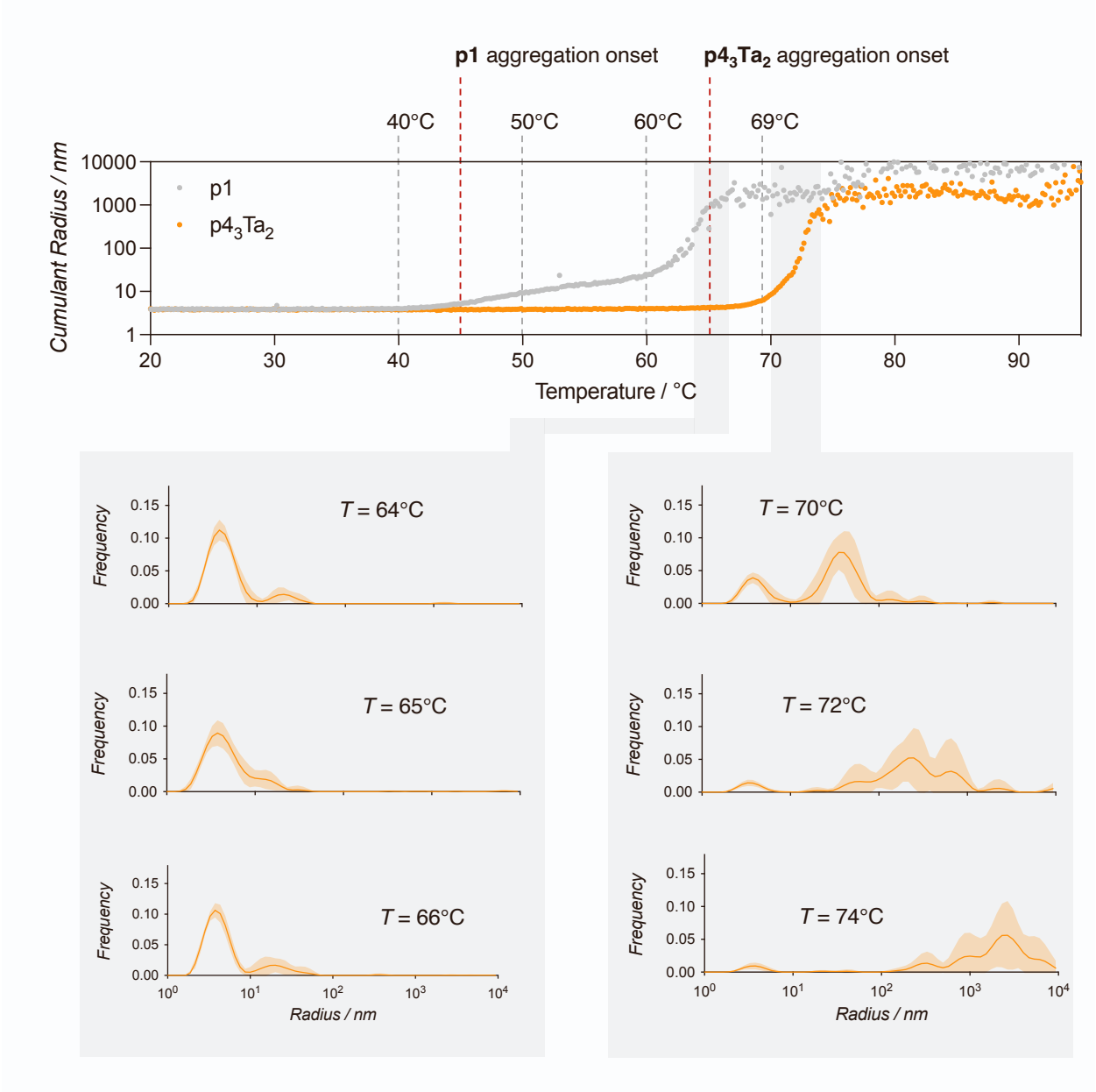

Figure S8. Crosslinked PFE DLS analysis shows aggregation resistance (relates to Figure 3C). Cumulant radius values determined by dynamic light scattering for **p1** (grey) and **p4₃Ta₂** (orange) demonstrate the predominant particle size of each protein between 20–95°C. Higher order **p1** oligomers begin to form above 45°C, whereas **p4₃Ta₂** remains monodisperse until 65°C (size distribution analysis for **p4₃Ta** at this temperature reveals some polydispersity that is not apparent from the cumulant radius value, which identifies only the dominant species). Temperatures for the initial onset of aggregation are indicated (dashed, red), as are the size distribution slices presented in Figure 3C (dashed, grey) with standard deviation shaded. Additional size distribution slices are shown for **p4₃Ta₂** at 64°C, 65°C, 66°C (showing initial aggregation onset) and at 70°C, 72°C, 74°C (showing complete aggregation). Each curve represents an average of six measurements within *T*+0.95°C of the given temperature.

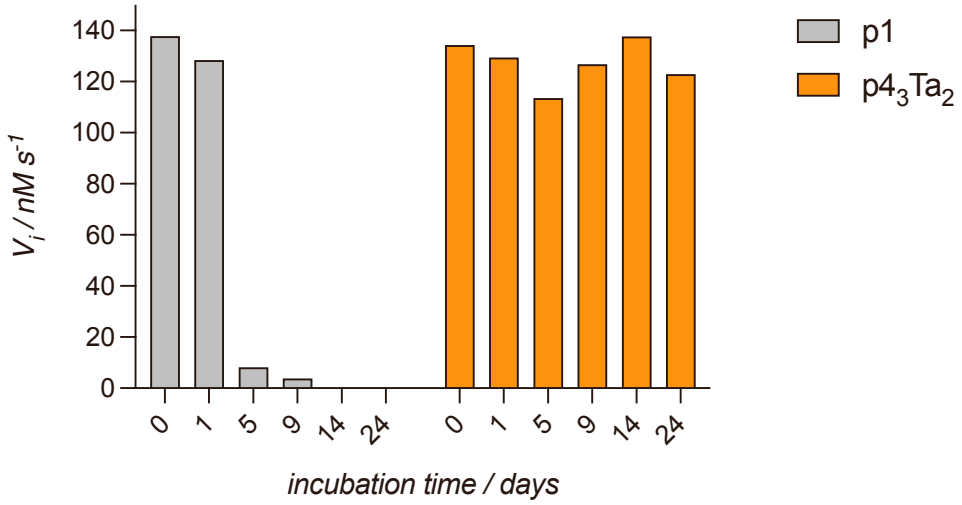

Figure S9. Long term temperature resistance of p4$_3$Ta$_2$. Hydrolysis activity of PFE variants **p1** and bicyclic **p4$_3$Ta$_2$** shows retained of activity of the crosslinked protein after more than three weeks of incubation at 50°C in 50 mM HEPES, 50 mM NaCl, pH 8.

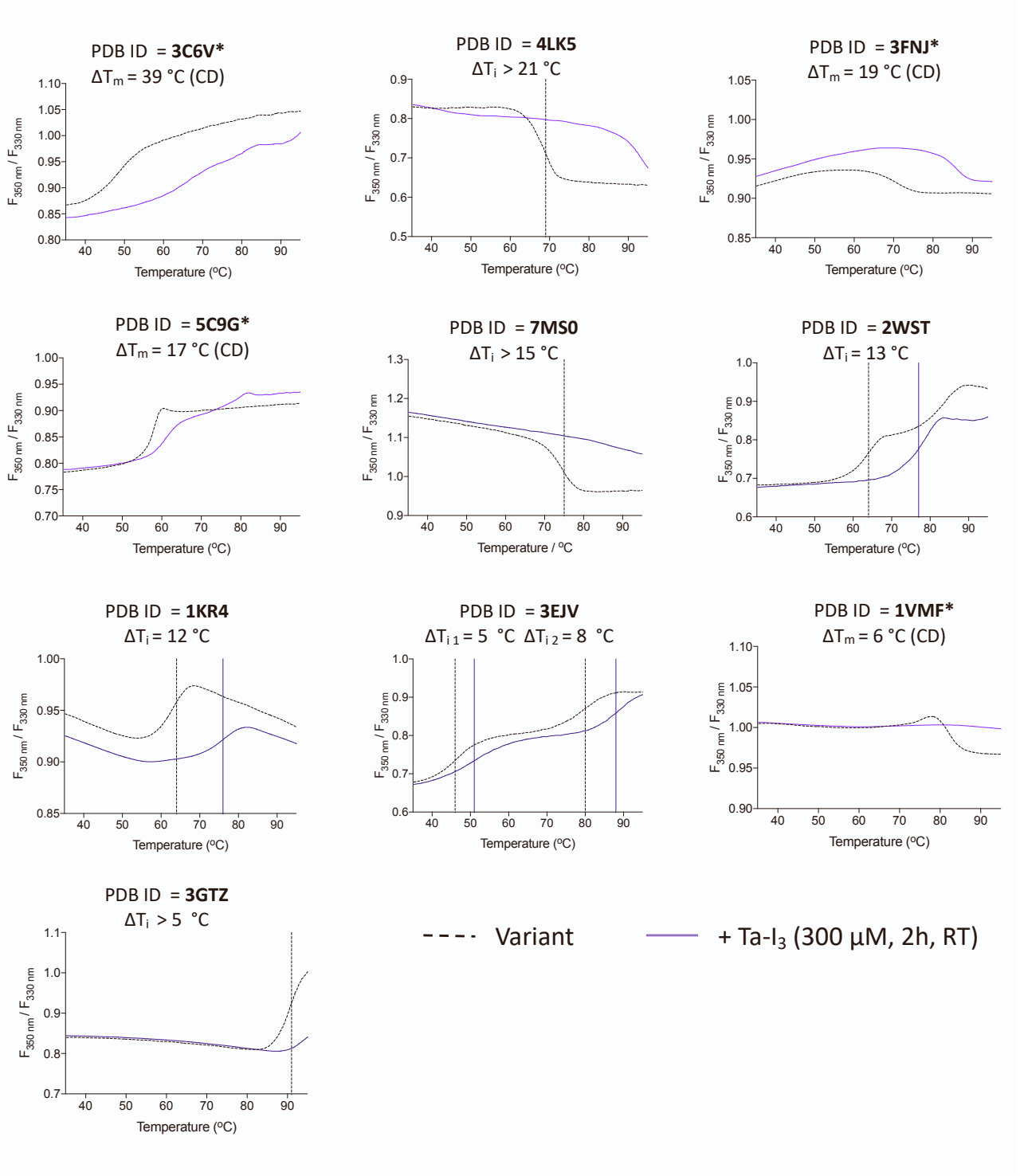

Figure S10. Widespread trimer stabilization by triselectrophile addition. DSF thermal denaturation measurements for the ten trimeric designs which demonstrated a stabilizing effect after addition of the crosslinker Ta-I_3 ($\Delta T_i > 5$°C). The bicyclized products of proteins derived from PDB IDs 3C6V, 5C9G, 3FNJ and 1VMF were further characterized and are presented in Figure 5. For these four examples, the T_m values indicated here were derived from circular dichroism (CD) measurements (Figure 5), whilst the T_i values for all other designs were determined by DSF.

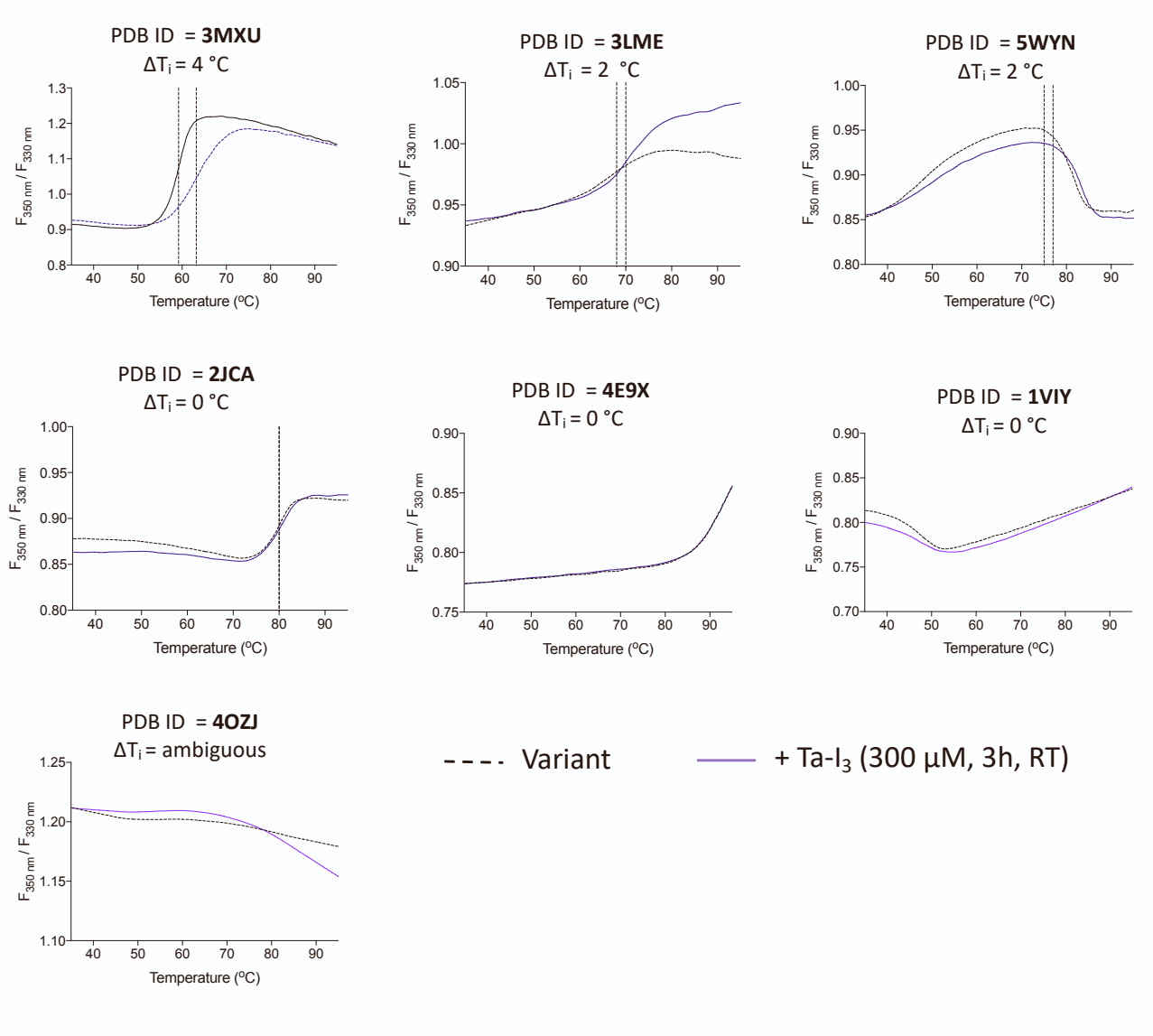

Figure S11. Unsuccessful stabilization of trimer variants. DSF thermal melt measurements of the seven tested designs for trimer crosslinking which failed to show a stabilization effect upon addition of the tris-electrophilic crosslinker Ta-I_3 (ΔT_i < 5°C).

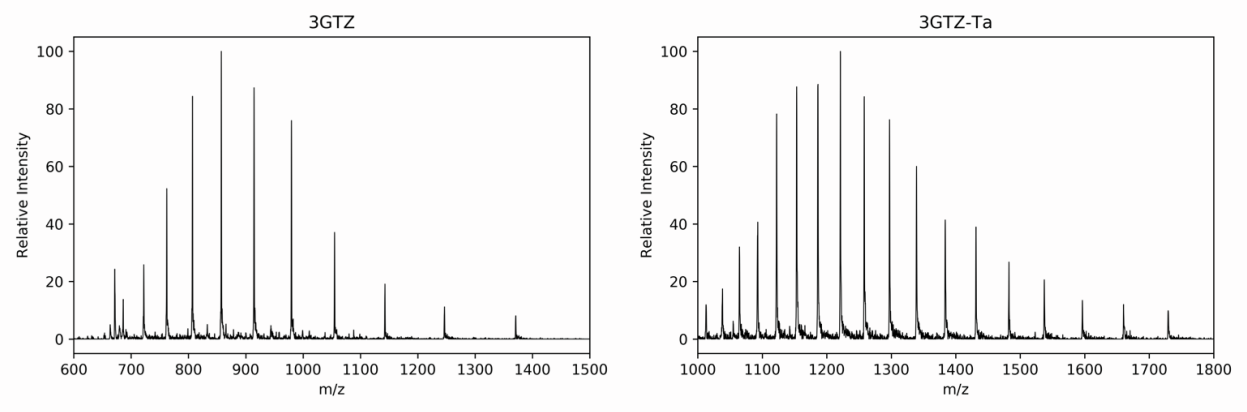

3GTZ (N20C & Q96C)
MW calc. = 13 700.5 Da
found = 13 701.5 Da

Charge	m/z found $[M+H]^+$	m/z calc.
20	686.3	686.0
19	722.1	722.1
18	762.2	762.1
17	807.1	806.9
16	857.3	857.3
15	914.5	914.4
14	979.7	979.6
13	1054.9	1054.9
12	1142.8	1142.7
11	1246.7	1246.5
10	1371.0	1371.1

Un-reacted 3GTZ peak list

single-crosslinked*:* **$3GTZ_3Ta_1$**
MW calc. = 41 479.9 Da Da
found. = 41 482.7 Da

Charge	m/z found $[M+H]^+$	m/z calc.
39	1064.6	1064.6
38	1092.6	1092.6
37	1122.3	1122.1
36	1153.3	1153.2
35	1186.1	1186.1
34	1221.1	1221.0
33	1258.1	1258.0
32	1297.3	1297.2
31	1339.2	1339.1
30	1383.7	1383.7
29	1431.4	1431.3
28	1482.5	1482.4
27	1537.3	1537.3
26	1596.4	1596.4
25	1660.2	1660.2

$3GTZ_3Ta_1$ peak list

Figure S12. Mass spectra of 3GTZ (N20C & Q96C) before (left) and after (right) addition of the crosslinker Ta-I_3, and peak lists for the un-reacted protein and single-crosslinked covalent trimer formed ($3GTZ_3Ta_1$). The molecular weight of the crosslinked version corresponds to the mass of three monomers of the un-reacted protein variant (13,700.5 Da) plus only one molecule of reacted Ta-I_3 (381.37 Da), minus the hydrogen atoms of the three cysteine thiols. The failure of the second crosslinking site suggests possible solvent inaccessibility of the introduced cysteine side chains. Despite the failure to bicyclize, thermal stabilization (ΔT_i > 5°C, Figure S10) is observed for the mono-crosslinked trimer. Data collected on Agilent LC/MSD XT ESI-Quadrupole LC/MS.

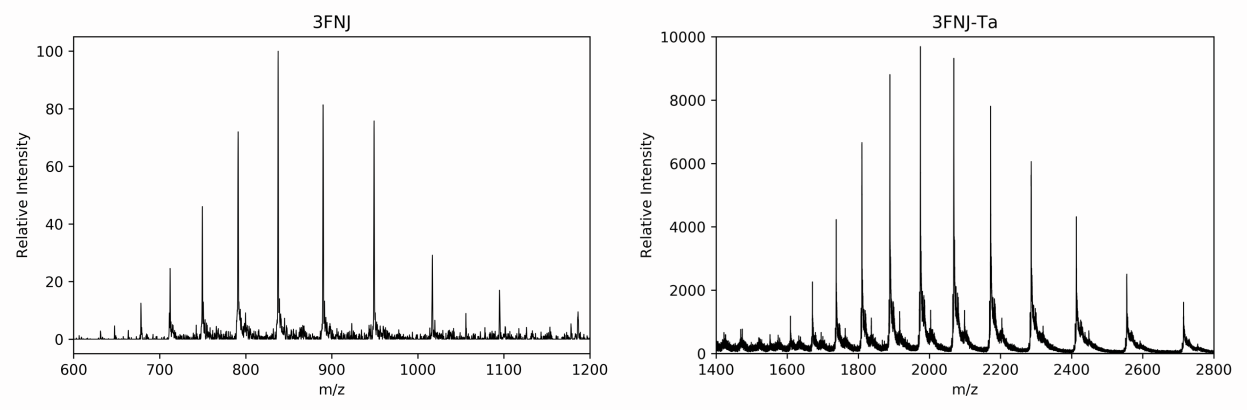

I4 (3FNJ, E7C & E108C)
MW calc. = 14 221.4 Da
found = 14 222.8 Da

bicyclic **I4$_3$Ta$_2$**
MW calc. = 43 420.9 Da
found. = 43 421.1 Da

Charge	m/z found $[M+H]^+$	m/z calc.
21	678.2	678.3
20	712.1	712.2
19	749.6	749.6
18	791.2	791.2
17	837.7	837.6
16	889.9	889.9
15	949.2	949.2
14	1016.9	1016.9
13	1094.9	1095.1
12	1186.2	1186.3

Un-reacted I4 peak list

Charge	m/z found $[M+H]^+$	m/z calc.
27	1609.19	1609.18
26	1671.11	1671.03
25	1737.85	1737.84
24	1810.22	1810.2
23	1888.88	1888.87
22	1974.7	1974.68
21	2068.68	2068.66
20	2171.94	2172.05
19	2286.32	2286.31
18	2413.33	2413.27
17	2555.25	2555.17
16	2714.85	2714.81

$I4_3Ta_2$ peak list (43 421.1 Da species)

Figure S13. Mass spectra and peak lists for I4 (PDB ID: 3FNJ, E7C & E108C) before (left) and after (right) crosslinking with two Ta-I$_3$ molecules, producing bicyclic **I4$_3$Ta$_2$** (Figure 5A). The found mass of **I4$_3$Ta$_2$** corresponds to the molecular weight of three copies of the un-reacted protein variant (14 221.4 Da) plus two molecules of reacted Ta (381.37 Da), minus six hydrogens. Data collected on Agilent LC/MSD XT ESI-Quadrupole LC/MS (**I4**) and Agilent 6230 ESI-TOF LC/MS (**I4$_3$Ta$_2$**).

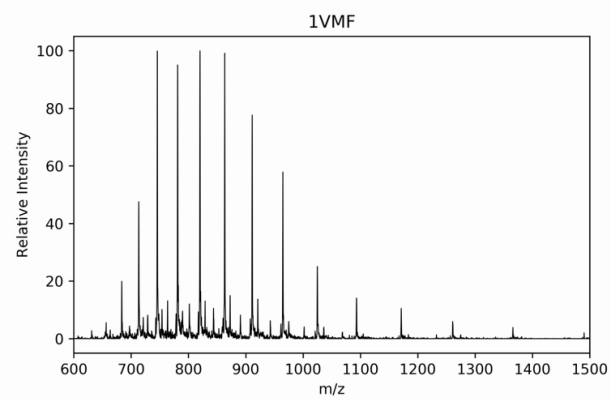

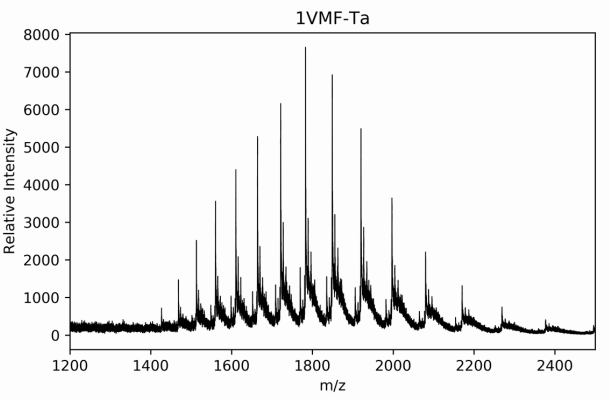

b4 (1VMF, E66C & T132C)
MW calc. = 16 381.5 Da
found = 16 383.6 Da

Charge	m/z found $[M+H]^+$	m/z calc.
24	683.8	683.6
23	713.3	713.2
22	745.7	745.6
21	781.2	781.1
20	820.2	820.1
19	863.3	863.2
18	911.2	911.1
17	964.7	964.6
16	1024.9	1024.8
15	1093.2	1093.1
14	1171.2	1171.1
13	1261.0	1261.1
12	1366.1	1366.1

Un-reacted b4 peak list

bicyclic **$b4_3Ta_2$**
MW calc. = 49 901.1 Da
found. = 49 901.1 Da

Charge	m/z found $[M+H]^+$	m/z calc.
35	1426.85	1426.75
34	1468.60	1468.68
33	1513.13	1513.15
32	1560.42	1560.41
31	1610.69	1610.71
30	1664.37	1664.37
29	1721.72	1721.73
28	1783.17	1783.18
27	1849.18	1849.19
26	1920.23	1920.27
25	1996.96	1997.04
24	2080.16	2080.21
23	2170.60	2170.61
22	2269.20	2269.23
21	2377.25	2377.24

$b4_3Ta_2$ peak list (49 901.1 Da species)

Figure S14. Mass spectra and peak lists for b4 (PDB ID: 1VMF, E66C & T132C) before (left) and after (right) crosslinking by two Ta-I_3 molecules, producing bicyclic **$b4_3Ta_2$** (Figure 5B). The found mass corresponds to the molecular weight of three copies of the un-reacted protein variant (16 381.5 Da) plus two molecules of reacted Ta (381.37 Da), minus six hydrogens. An additional species with a mass difference of approximately +178 Da (*MW* = 16 561 Da) was observed for the un-reacted protein, corresponding to a common post-translational gluconylation of the protein N-terminus [6]. This mass increase becomes more prominent in the subsequent spectra of the covalently cross-linked trimer due to the probability of at least one gluconylated monomer forming part of a trimer (*MW* = 50 079 Da). Data collected on Agilent LC/MSD XT ESI-Quadrupole LC/MS (**b4**) and Agilent 6230 ESI-TOF LC/MS (**$b4_3Ta_2$**).

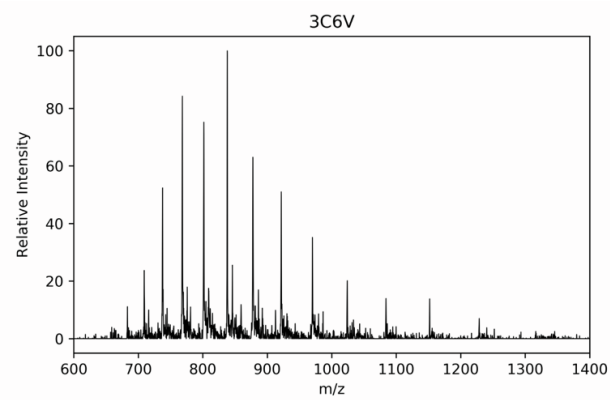

a4 (3C6V, E45C & A70C)
MW calc. = 18 411.8 Da
found = 18 413.7 Da

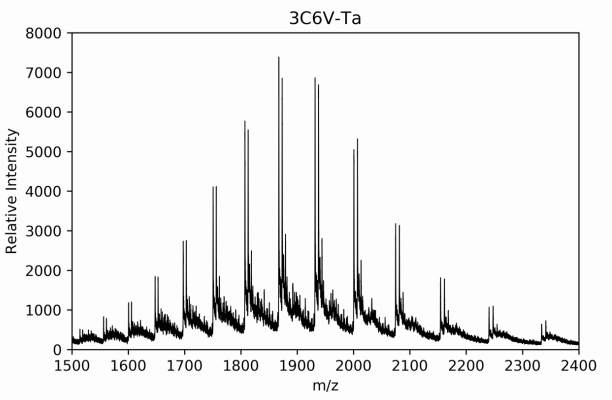

bicyclic **a4$_3$Ta$_2$**
MW calc. = 55 992.1 Da
found. = 55 991.7 Da

Charge	m/z found $[M+H]^+$	m/z calc.
27	683.3	682.9
26	709.2	709.1
25	737.7	737.5
24	768.4	768.2
23	801.7	801.5
22	838.0	837.9
21	877.7	877.8
20	921.7	921.6
19	970.0	970.0
18	1024.1	1023.9
17	1084.1	1084.0
16	1151.9	1151.7

Un-reacted a4 peak list

Charge	m/z found $[M+H]^+$	m/z calc.
36	1556.28	1556.34
35	1600.77	1600.77
34	1647.85	1647.83
33	1697.67	1697.73
32	1750.76	1750.75
31	1807.21	1807.20
30	1867.41	1867.40
29	1931.77	1931.76
28	2000.74	2000.72
27	2074.79	2074.78
26	2154.55	2154.54
25	2240.70	2240.68
24	2333.98	2334.00

$a4_3Ta_2$ peak list (55 991.7 Da species)

Figure S15. Mass spectra and peak lists for a4 (PDB ID: 3C6V, E45C & A70C) before (left) and after (right) crosslinking by two Ta-I$_3$ molecules, producing bicyclic **a4$_3$Ta$_2$** (Figure 5C). The found mass corresponds to the molecular weight of three copies of the un-reacted protein variant (18 411.8 Da) plus two molecules of reacted Ta (381.37 Da), minus six hydrogens. An additional species with a mass difference of approximately +178 Da (*MW* = 18 592 Da) was observed for the un-reacted protein, corresponding to a common post-translational gluconylation of the protein N-terminus [6]. This mass increase becomes more prominent in the subsequent spectra of the covalently cross-linked trimer due to the probability of at least one gluconylated monomer forming part of a trimer (*MW* = 56 170). Data collected on Agilent LC/MSD XT ESI-Quadrupole LC/MS (**a4**) and Agilent 6230 ESI-TOF LC/MS (**a4$_3$Ta$_2$**).

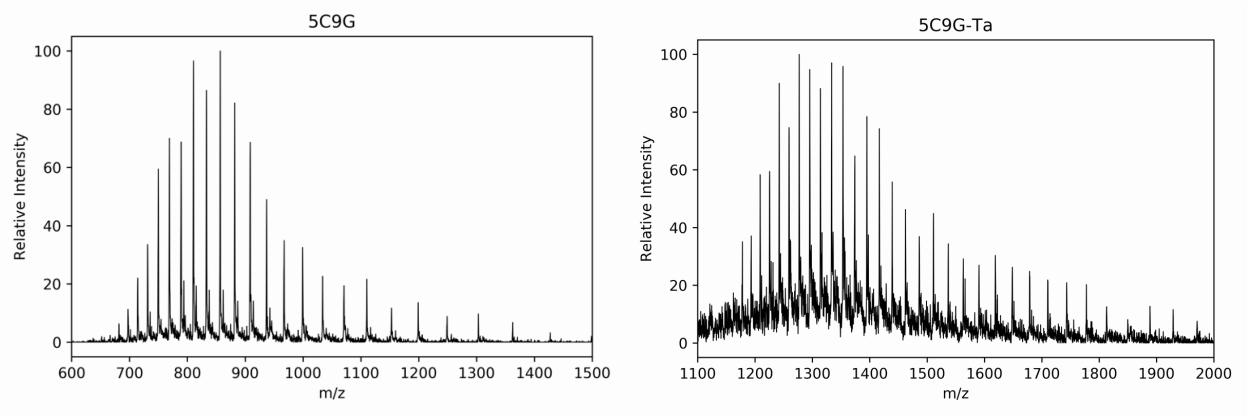

e4 (5C9G, S176C & G221C)
MW calc. = 29 951.1 Da
found = 29 952.9 Da

bicyclic **e4$_3$Ta$_2$**
MW calc. = 90 610.1 Da
found. = 90 606.7 Da

Charge	m/z found $[M+H]^+$	m/z calc.
41	731.4	731.5
40	749.8	749.8
39	769.1	769.0
38	789.3	789.2
37	810.6	810.5
36	833.0	833.0
35	856.9	856.7
34	882.0	881.9
33	908.8	908.6
32	937.1	937.0
31	967.4	967.2
30	999.4	999.4
29	1034.0	1033.8
28	1079.9	1070.7
27	1110.4	1110.3
26	1153.2	1153.0
25	1199.2	1199.0
24	1249.2	1249.0

Un-reacted e4 peak list

Charge	m/z found $[M+H]^+$	m/z calc.
74	1225.4	1225.5
73	1242.2	1242.2
72	1259.3	1259.5
71	1277.0	1277.2
70	1295.4	1295.4
69	1314.0	1314.2
68	1333.7	1333.5
67	1353.4	1353.4
66	1374.1	1373.9
65	1395.0	1395.0
64	1416.7	1416.8
63	1439.2	1439.3
62	1462.3	1462.5
61	1486.3	1486.4
60	1511.2	1511.2
59	1537.1	1536.8
58	1563.2	1563.2
57	1590.6	1590.7

$e4_3Ta_2$ peak list (90 606.7 Da species)

Figure S16. Mass spectra and peak lists for e4 (PDB ID: 5C9G, S176C & G221C) before (left) and after (right) crosslinking by two Ta-I$_3$ molecules, producing bicyclic **e4$_3$Ta$_2$** (Figure 5D). The found mass corresponds to the molecular weight of three copies of the un-reacted protein variant (29 951.1 Da) plus two molecules of reacted Ta (381.37 Da), minus six hydrogens. Data collected on Agilent LC/MSD XT ESI-Quadrupole LC/MS.

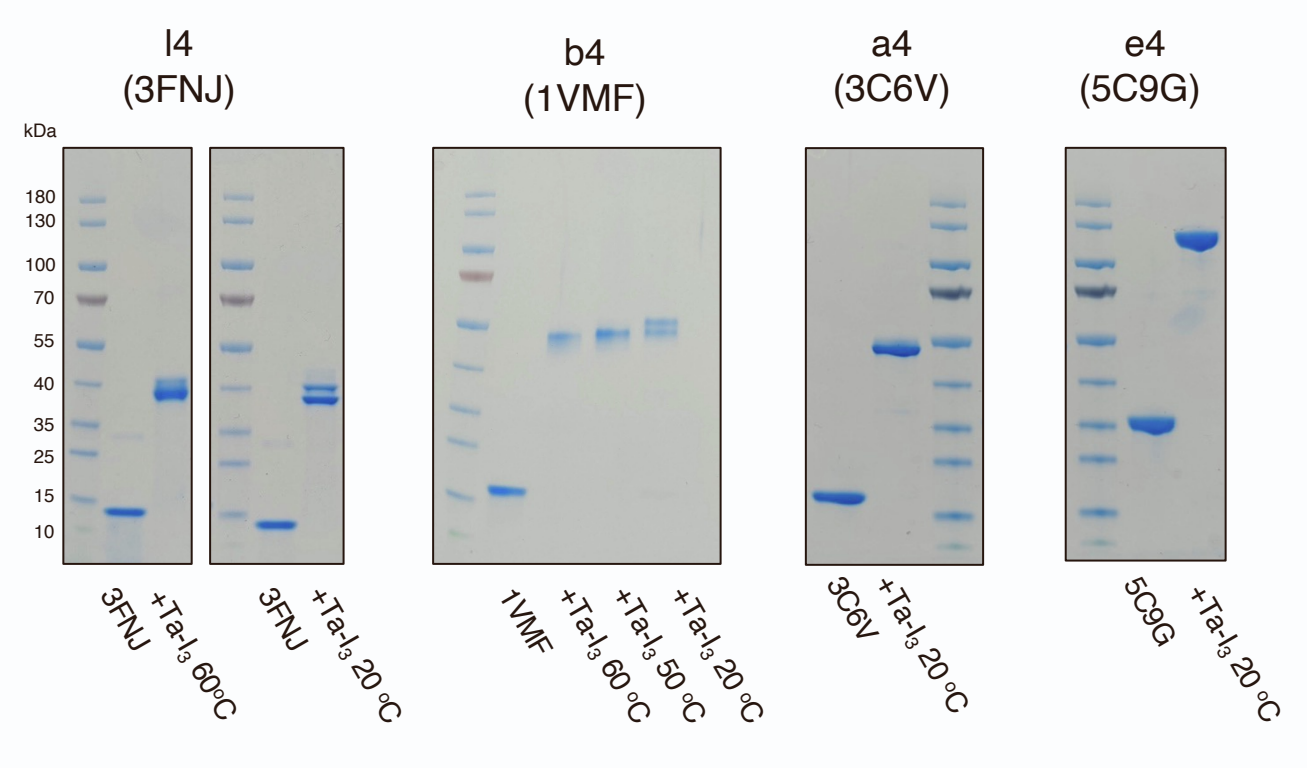

Variant	Expected MW monomer / kDa	Expected MW trimer / kDa
a4	18.4	56.0
e4	30.0	90.6
l4	14.2	43.4
b4	16.4	49.0

Figure S17. SDS-PAGE analysis of 2-hour reactions of Ta-l_3 with homotrimers shows formation of crosslinked species (relates to trimers presented in Figure 5). All four proteins demonstrate formation of a covalent trimer. In analogy to the bicyclic PFE variant (**$p4_3Ta_2$**), we observed migration behaviour deviating from the linear protein ladder (higher apparent masses) due to the altered protein chain topology. The reactions for **l4** (3FNJ) and **b4** (1VMF) at room temperature show evidence of two closely related species, however increasing the reaction temperature resolves both to a predominant single product. The crosslinked SDS-PAGE **b4** sample was prepared by addition of 6 M urea in addition to loading dye, and not heated to 95°C, as the standard protocol failed to migrate through the gel.

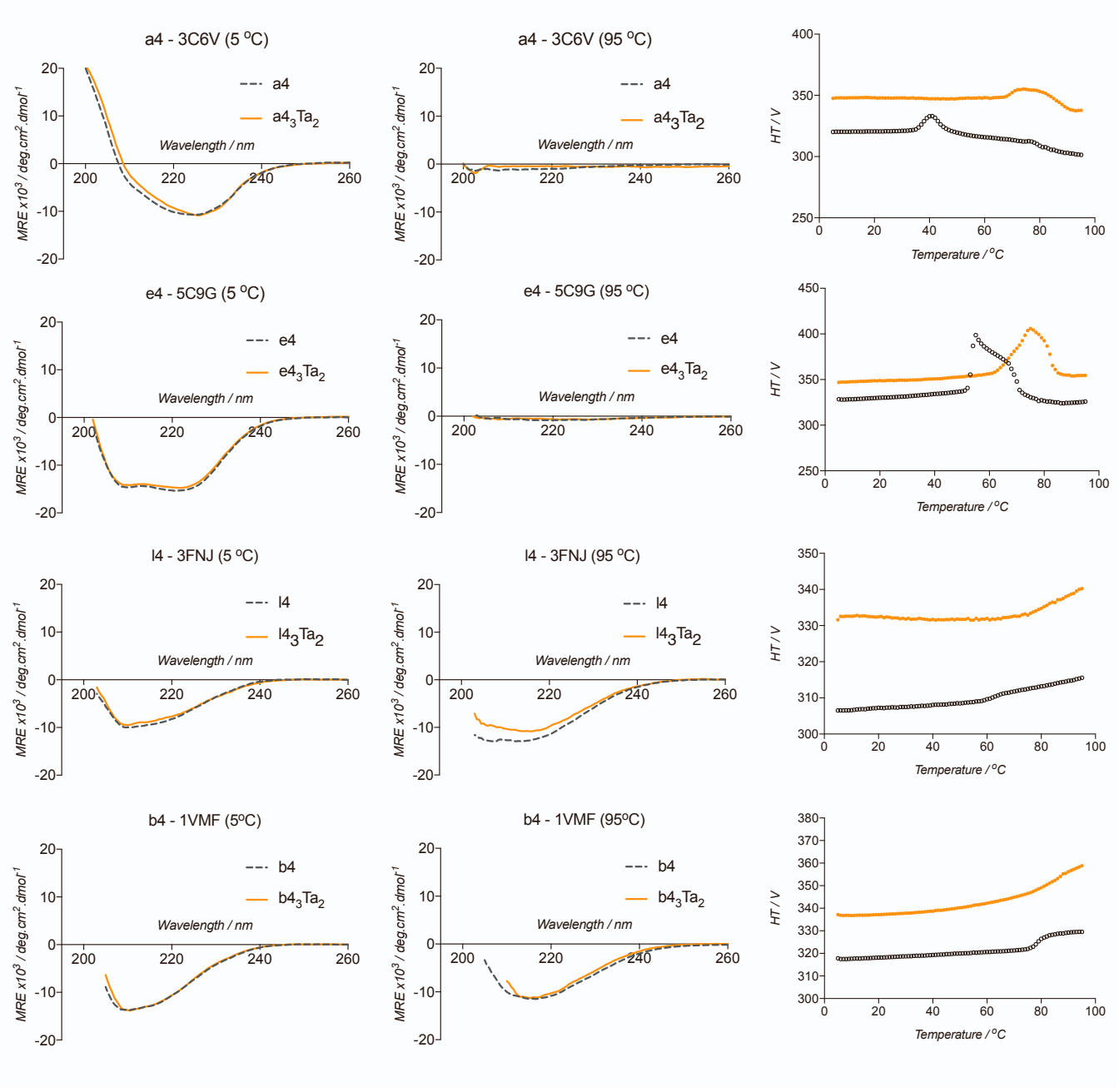

Figure S18. Circular dichroism validates stabilization of bicyclic trimers (relating to data presented in Figure 5). Circular dichroism spectra (λ = 200–260 nm) of trimeric variants before (black, dash) and after (orange) crosslinking, at 5°C (left) and 95°C (middle). Right: High tension (HT) recordings for thermal denaturation measurements (λ = 220).

Supplementary Tables

Table S1. High-resolution native MS of PFE trimers. Includes **p1** and crosslinked trimer variants **p2$_3$Ta**, **p3$_3$Ta** and **p4$_3$Ta$_2$**. Data collected on TIMS-Qq-TOF mass spectrometer with an ESI source.

Sample	Calculated mass trimer (*MW* / Da)	Found (*m*/*z*, with *z* = 20$^+$)	Deconvoluted (*MW* / Da)	Mass accuracy (ppm)
p1	92784.00	4640.12	92783.15	-9 ppm
p2$_3$Ta	93168.44	4659.73	93167.10	-14 ppm
p3$_3$Ta	93087.38	4655.59	93086.20	-9.4 ppm
p4$_3$Ta	93471.82	4674.83	93469.89	-20 ppm

Table S2. Peak list for MS charge state analysis of p2$_3$Ta. Most abundant charge state is Z = 91 (Figure 1C). Data collected on Agilent Technologies G6230A ESI-TOF LC/MS.

Charge	m/z found $[M+H]^+$	Relative Abundance	Charge	m/z found $[M+H]^+$	Relative Abundance
114	818.20	0.029	79	1180.27	0.522
113	825.42	0.041	78	1195.38	0.492
111	840.28	0.053	77	1210.89	0.482
110	847.90	0.074	76	1226.81	0.483
109	855.68	0.096	75	1243.15	0.473
108	863.59	0.111	74	1259.94	0.488
107	871.64	0.139	73	1277.19	0.470
106	879.86	0.172	72	1294.91	0.469
105	888.24	0.209	71	1313.14	0.461
104	896.76	0.237	70	1331.88	0.445
103	905.47	0.292	69	1351.17	0.443
102	914.33	0.355	68	1371.04	0.421
101	923.38	0.417	67	1391.47	0.406
100	932.60	0.485	66	1412.54	0.402
99	942.02	0.578	65	1434.26	0.377
98	951.62	0.661	64	1456.70	0.352
97	961.42	0.758	63	1479.76	0.344
96	971.43	0.819	62	1503.61	0.310
95	981.64	0.893	61	1528.25	0.293
94	992.07	0.943	60	1553.71	0.268
93	1002.74	0.996	59	1580.02	0.253
92	1013.62	0.970	58	1607.25	0.233
91	**1024.75**	**1.000**	57	1635.42	0.209
90	1036.13	0.961	56	1664.61	0.194
89	1047.76	0.951	55	1694.85	0.177
88	1059.65	0.873	54	1726.22	0.157
87	1071.82	0.831	53	1758.77	0.145
86	1084.28	0.794	52	1792.58	0.123
85	1097.02	0.724	51	1827.71	0.111
84	1110.06	0.680	50	1864.25	0.099
83	1123.43	0.631	49	1902.27	0.084
82	1137.12	0.600	48	1941.88	0.069
81	1151.14	0.558	47	1983.17	0.058
80	1165.52	0.525	46	2026.28	0.047

Table S3. Peak list for MS charge state analysis of p3$_3$Ta. Most abundant charge state is Z = 61 (Figure 1C). Data collected on Agilent Technologies G6230A ESI-TOF LC/MS.

Charge	m/z found $[M+H]^+$	Relative Abundance	Charge	m/z found $[M+H]^+$	Relative Abundance
85	1096.11	0.008	58	1605.81	0.975
84	1109.05	0.006	57	1633.96	0.945
83	1122.38	0.009	56	1663.12	0.884
82	1136.05	0.019	55	1693.34	0.832
81	1150.13	0.016	54	1724.68	0.777
80	1164.52	0.020	53	1757.20	0.711
79	1179.19	0.031	52	1790.98	0.631
78	1194.32	0.042	51	1826.07	0.562
77	1209.81	0.053	50	1862.57	0.504
76	1225.7	0.074	49	1900.57	0.444
75	1242.05	0.093	48	1940.14	0.393
74	1258.82	0.119	47	1981.40	0.340
73	1276.06	0.152	46	2024.46	0.291
72	1293.76	0.200	45	2069.42	0.239
71	1311.97	0.248	44	2116.43	0.192
70	1330.7	0.312	43	2165.63	0.159
69	1349.96	0.389	42	2217.16	0.131
68	1369.8	0.469	41	2271.22	0.108
67	1390.24	0.575	40	2327.97	0.090
66	1411.29	0.692	39	2387.64	0.074
65	1432.98	0.769	38	2450.44	0.062
64	1455.35	0.868	37	2516.64	0.052
63	1478.45	0.932	36	2586.52	0.039
62	1502.28	0.970	35	2660.40	0.027
61	**1526.88**	**1.000**	34	2738.63	0.018
60	1552.32	0.999	33	2821.58	0.011
59	1578.61	0.989	32	2909.88	0.006

Table S4. Peak list for MS charge state analysis of $p4_3Ta_2$. Most abundant charge state is Z = 42 (Figure 1C). Data collected on Agilent Technologies G6230A ESI-TOF LC/MS.

Charge	m/z found $[M+H]^+$	Relative Abundance
66	1417.20	0.023
63	1484.61	0.035
62	1508.50	0.042
61	1533.17	0.058
60	1558.73	0.064
59	1585.09	0.080
58	1612.39	0.104
57	1640.67	0.132
56	1669.95	0.156
55	1700.28	0.192
54	1731.75	0.233
53	1764.39	0.277
52	1798.31	0.326
51	1833.55	0.383
50	1870.20	0.446
49	1908.34	0.508
48	1948.08	0.574
47	1989.50	0.647
46	2032.74	0.722
45	2077.88	0.808
44	2125.09	0.889
43	2174.48	0.970
42	**2226.23**	**1.000**
41	2280.50	0.980
40	2337.49	0.888
39	2397.41	0.757
38	2460.47	0.621
37	2526.95	0.485
36	2597.12	0.381
35	2671.31	0.295
34	2749.85	0.246
33	2833.15	0.204
32	2921.66	0.170

Table S5. Peak lists for MS charge state analysis of un-reacted p2, p3 and p4. Most abundant charge states are 37, 37 and 38 respectively. Data collected on Agilent Technologies G6230A ESI-TOF LC/MS.

p2

Charge	m/z found $[M+H]^+$	Relative Abundance
47	659.0	1686
46	673.3	3526
45	688.3	7620
44	703.9	16883
43	720.2	34836
42	737.4	73319
41	755.3	139003
40	774.2	208155
39	794.0	276399
38	814.9	319631
37	**836.9**	**330838**
36	860.1	314184
35	884.6	283557
34	910.6	253840
33	938.2	222451
32	967.5	194658
31	998.6	169614
30	1031.9	143373
29	1067.4	122401
28	1105.5	102762
27	1146.4	90941
26	1190.5	85006
25	1238.1	81834
24	1289.6	83511
23	1345.6	85830
22	1406.8	80611
21	1473.7	62805
20	1547.3	37650
19	1628.7	17555
18	1719.2	8198
17	1820.2	4385
16	1933.9	2530

p3

Charge	m/z found $[M+H]^+$	Relative Abundance
44	703.3	310
43	719.6	549
42	736.7	1083
41	754.7	1871
40	773.5	2638
39	793.3	3720
38	814.2	4391
37	**836.2**	**4919**
36	859.4	4820
35	883.9	4535
34	909.9	4098
33	937.4	3641
32	966.7	3317
31	997.8	3012
30	1031.0	2446
29	1066.6	2211
28	1104.6	1756
27	1145.5	1574
26	1189.5	1419
25	1237.1	1422
24	1288.6	1401
23	1344.5	1464
22	1405.6	1365
21	1472.5	1084
20	1546.1	691
19	1627.4	325

p4

Charge	m/z found $[M+H]^+$	Relative Abundance
45	687.8	377
44	703.4	575
43	719.7	1139
41	754.8	2929
40	773.6	5755
39	793.4	8270
38	**814.3**	**9580**
37	836.3	9069
36	859.5	9763
35	884.0	9723
34	910.0	9134
33	937.5	8188
32	966.8	7341
31	997.9	5153
30	1031.2	5660
29	1066.7	4647
28	1104.7	3492
27	1145.6	3667
26	1189.7	2481
25	1237.2	3149
24	1288.7	2859
23	1344.7	2881
22	1405.8	2480
21	1472.6	1993
20	1546.2	1217
19	1627.6	619
18	1717.9	314

Table S6. **Thermal stabilization of crosslinked PFE variants.** Inflection melting temperatures (T_i) for PFE variants **p1**-**p4** and their crosslinked variants. Values are an average of triplicate DSF measurements, T_i values are not reported where the dynamic range of the measurement is less than 30% of the corresponding native melt (melting curves presented in Figure 2B, 2C and Figure S5).

	Native T_i / °C	**Denaturing T_i / °C**			
	0.0 M GuHCl	0.5 M GuHCl	1.0 M GuHCl	1.5 M GuHCl	2.0 M GuHCl
p1	79.6	62.0	52.6	-	-
p2	79.7	62.3	52.9	-	-
p3	76.9	59.3	-	-	-
p4	76.8	59.3	-	-	-
$p2_3Ta$	80.6	65.0	54.6	-	-
$p3_3Ta$	84.3	67.7	57.3	51.2	-
$p4_3Ta_2$	85.2	70.9	61.6	53.0	-

Table S7. Denaturant resistant activity of crosslinked PFE variants (relates to Figure 2D). Initial rates of *p*-NPA hydrolysis by PFE variants (errors account for 1σ). Initial rate values determined from curves presented in Figure 2E, 2F and Figure S6. The relative rates (relative to the initial **$p4_3Ta_2$** rate at each given GuHCl concentration) are presented in Figure 2D.

	p1		**$p2_3Ta$**		**$p3_3Ta$**		**$p4_3Ta_2$**	
Concentration of GuHCl / M	**Initial rate / mM.s^{-1}**	**Error**	**Initial rate / mM.s^{-1}**	**Error**	**Initial rate / mM.s^{-1}**	**Error**	**Initial rate / mM.s^{-1}**	**Error**
0.0	$1.06 \cdot 10^{-3}$	$0.16 \cdot 10^{-3}$	$1.28 \cdot 10^{-3}$	$0.14 \cdot 10^{-3}$	$1.14 \cdot 10^{-3}$	$0.17 \cdot 10^{-3}$	$1.25 \cdot 10^{-3}$	$0.13 \cdot 10^{-3}$
0.5	$5.57 \cdot 10^{-4}$	$0.13 \cdot 10^{-4}$	$5.48 \cdot 10^{-4}$	$0.12 \cdot 10^{-4}$	$6.27 \cdot 10^{-4}$	$0.093 \cdot 10^{-4}$	$5.97 \cdot 10^{-4}$	$0.15 \cdot 10^{-4}$
1.0	$2.78 \cdot 10^{-4}$	$0.053 \cdot 10^{-4}$	$3.65 \cdot 10^{-4}$	$0.088 \cdot 10^{-4}$	$3.38 \cdot 10^{-4}$	$0.068 \cdot 10^{-4}$	$3.45 \cdot 10^{-4}$	$0.19 \cdot 10^{-4}$
1.5	$7.08 \cdot 10^{-6}$	$0.79 \cdot 10^{-6}$	$9.89 \cdot 10^{-5}$	$0.091 \cdot 10^{-5}$	$1.52 \cdot 10^{-4}$	$0.027 \cdot 10^{-4}$	$2.03 \cdot 10^{-4}$	$0.052 \cdot 10^{-4}$
2.0	$5.74 \cdot 10^{-7}$	$0.40 \cdot 10^{-7}$	$1.36 \cdot 10^{-5}$	$0.18 \cdot 10^{-5}$	$5.36 \cdot 10^{-5}$	$0.14 \cdot 10^{-5}$	$7.52 \cdot 10^{-5}$	$0.30 \cdot 10^{-5}$

Table S8. Data collection and structural refinement statistics for bicyclic $p4_3Ta_2$. Values in parentheses represent the highest resolution shell (2.50–2.60 Å). Crystal structure presented in Figure 4.

	$p4_3Ta_2$ (PDB ID = 8pi1)
Data Collection	
Beamline	Diamond Light Source, I04
Space group	C 1 2 1
Unit cell dimensions (Å): a, b, c	254.80, 146.25, 154.59
Unit cell angles (°): a, b, g	90.00, 122.63, 90.00
Resolution (Å)	2.50
Number of unique reflections	164678
$CC_{1/2}$	99.7 *(52.1)*
I/σ	8.88 *(1.12)*
Completeness (%)	100.0 *(99.9)*
Refinement	
Resolution (Å)	2.50
No. unique reflections used in refinement	156444
R_{work}	0.182
R_{free}	0.224
No. protein atoms used in refinement	31 894
No. water molecules used in refinement	533
Average B-factors (Å^2)	45.25
R.M.S deviations – length (Å)	0.010
R.M.S deviations – angle (°)	1.320
Ramachandran favoured residues (%)	97
Ramachandran outlying residues (%)	0

Table S9. PDB ID codes of 119 proteins identified by search for non-redundant C3-symmetric protein trimers. Each contains up to one cysteine residue and at least one tryptophan per monomer, as well as a hexa-histidine tag in their PDB sequence.

No.	PDB	Cys	No.	PDB_ID	Cys	No.	PDB	Cys	No.	PDB	Cys
1	6T6J	0	**32**	4UMI	0	**63**	2JCA	0	**94**	5WYN	1
2	2CZ4	0	**33**	5BOH	0	**64**	3ZEZ	1	**95**	4F3J	1
3	3FNJ	0	**34**	4PXK	0	**65**	7MS0	1	**96**	4UAH	1
4	3LME	0	**35**	5KKH	0	**66**	4OZJ	1	**97**	6YZY	1
5	3H5I	0	**36**	4XXJ	0	**67**	4E9X	1	**98**	4EX8	1
6	2WDY	0	**37**	6XT4	0	**68**	3T9W	1	**99**	3ZE3	1
7	3MXU	0	**38**	4UC0	0	**69**	5TB7	1	**100**	6YSP	1
8	4D0V	0	**39**	3E35	0	**70**	4XI0	1	**101**	4LHR	1
9	3I7T	0	**40**	2ETV	0	**71**	7RFO	1	**102**	4OUS	1
10	4JCU	0	**41**	2WAM	0	**72**	4XC5	1	**103**	4OUL	1
11	3Q8U	0	**42**	6EUS	0	**73**	4NJN	1	**104**	1VMH	1
12	3C6V	0	**43**	5KA6	0	**74**	6PSP	1	**105**	4M1A	1
13	5B8F	0	**44**	3K9A	0	**75**	5C9G	1	**106**	3OFV	1
14	5XUB	0	**45**	5APZ	0	**76**	3GVF	1	**107**	3B8L	1
15	6B7C	0	**46**	2IBL	0	**77**	5WUF	1	**108**	2RDM	1
16	4GCY	0	**47**	5ZHY	0	**78**	2NT8	1	**109**	4DI1	1
17	3EJV	0	**48**	5LNL	0	**79**	4LK5	1	**110**	4NSN	1
18	3ZF1	0	**49**	4Y2L	0	**80**	3H0U	1	**111**	5N2C	1
19	1VIY	0	**50**	3LYB	0	**81**	2WST	1	**112**	4HZ5	1
20	7DSZ	0	**51**	2YO2	0	**82**	2DCH	1	**113**	3AM2	1
21	5WUC	0	**52**	3BK6	0	**83**	3GTZ	1	**114**	3ZJB	1
22	1PG6	0	**53**	3WPP	0	**84**	1VPH	1	**115**	3K12	1
23	4G9Q	0	**54**	3QV0	0	**85**	4XEL	1	**116**	4L8P	1
24	6ZLO	0	**55**	3LX2	0	**86**	1VMF	1	**117**	7E4G	1
25	3GKB	0	**56**	2XQH	0	**87**	2YKP	1	**118**	2B2H	1
26	2PBZ	0	**57**	6H21	0	**88**	2YKO	1	**119**	5KVB	1
27	5O68	0	**58**	2C3F	0	**89**	1KR4	1			
28	1LR0	0	**59**	4USX	0	**90**	1VHF	1			
29	4LKB	0	**60**	5HRZ	0	**91**	3RPX	1			
30	4EC6	0	**61**	4LGO	0	**92**	4LEH	1			
31	2F1V	0	**62**	5WTR	0	**93**	4L8O	1			

Table S10. Bicyclization via Ta-I_3 was attempted for 14 unique CATH domains, of which variants for 13 domains were successfully expressed and purified. Eight domains demonstrated significant thermal stabilization after addition of the crosslinker, while bicyclization was confirmed for four examples (*) by mass spectrometry (Figures S13–S16). **Indicates T_m values (equilibrium midpoint) obtained by circular dichroism measurements (Figure 5), all other values indicate T_i (inflection temperature) obtained by DSF measurements (Figures S10 and S11). Sequences are provided in (Table S11).

No.	CATH Domain	Domain name	PDB ID (variant)	Crosslinking Sites	Variant T_i / °C	Crosslinked T_i / °C	ΔT_i / °C
1	3.30.429.10	Macrophage Migration Inhibitory Factor	3C6V* (a4)	*E45C & A70C*	41	80	39**
			7MS0	*R10C & E107C*	75	>90	>15
2	3.90.226.10	2-enoyl-CoA Hydratase	5C9G* (e4)	*S176C & G221C*	54	71	17**
			4LK5	*A185C & E231C*	69	>90	>21
3	3.40.250.10	Rhodanese-like domain	3FNJ* (I4)	*E7C & E108C*	61	80	19**
4	2.60.120.460	YjbQ-like, Jelly Rolls, Sandwich	1VMF* (b4)	*E66C & T132C*	77	83	6**
5	2.60.90.10	Adenovirus pIV-related, attachment domain	2WST	*V117C & V245C*	64	77	13
6	3.30.70.120	Alpha-Beta Plaits	1KR4	*E34C & E86C*	64	76	12
			4OZJ	*N43C & E108C*	ambiguous	ambiguous	-
7	3.10.450.50	Nuclear Transport Factor 2	3EJV	*A4C & V126C*	46, 80	51, 88	5-8
8	3.30.1330.40	RutC-like	3GTZ	*N20C & Q96C*	90	>95	> 5
			3LME	*D53C & Q136C*	68	70	2
9	2.40.50.100	RNA polymers II, barrel-sandwich hybrid domain	3MXU	*D9C & A115C*	59	63	4
10	2.30.42.10	PDZ domain	5WYN	*Q146C & A327C*	76	78	2
11	3.40.50.300	P-loop containing NTP hydrolases	1VIY	*E79C & A167C*	ambiguous	ambiguous	0
12	3.90.470.20	4'-phosphopantetheinyl transferase domain	2JCA	*S2C & E12C*	80	80	0
13	2.60.40.420	Cupredoxins - blue copper proteins	4E9X	*M195&D254*	>90°C	>90°C	0
14	2.70.40.10	Deoxyuridine triphosphatase (dUTPase)	3ZEZ	*Y57C & K100C*	No expression	-	-

Table S11. Full-length sequences of the expanded suite of C3-symmetric trimer variants designed for bicyclization, including purification tags. All proteins were expressed in a pET28a (+) vector.

3FNJ_INCYPRO (l4)
MANDKKICLLTTYLSLYIDHHTVLADMQNATGKYVVLDVRNAPAQVKKDQIKGAIAMPAKDLATRIGELDPAKTYVV
YDWTGGTTLGKTALLVLLSAGFEAYELAGALCGWKGMQLPVETLADLEHHHHHH

3LME_INCYPRO
MASLKIIAPTDKTITPSGTWSIGARAGCFVFIGGMHGTDRVTGKMVDGDEARIRRMFDNMLAAAEAAGATKADAVRL
TVFVTDVAKYRPVVNKVQKDIWGDGPYPPRTVLCVPALDQGDIAEIDGTFYAPAEGHHHHHH

2JCA_INCYPRO
MGSSHHHHHHSSGLVPRGSHMCIIGVGIDVACVERFGAALERTPALAGRLFLESELLLPGGERRGVASLAARFAAKE
ALAKALGAPAGLLWTDAEVWVEAGGRPRLRVTGTVAARAAELGVASWHVSLSHDAGIASAVVIAEG

3MXU_INCYPRO
MAHHHHHHMGTLEAQTQGPGSMSKTYFTQCHEWLSVEGQVVTVGITDYAQEQLGDLVFIDLPQNGTKLSKGDAAAVV
ESVKAASDVYAPLDGEVVEINAALAESPELVNQKAETEGWLWKMTVQDETQLERLLDECAYKELIG

3C6V_INCYPRO (a4)
MGSSHHHHHHSSGRENLYFQGMPRWLIQHSPNTLTPEEKSHLAQQITQAYVGFGLPAFYVQVHFICQPAGTSFIGGE
QHPNFVALTIYHLCRTMTSDEQRQGFLKRIDAFLTPMFEPKGIDWEYFVTEAPRDLWKINGLAPPAAGSEEEKVWVR
ENRPVRF

3EJV_INCYPRO
MGSDKIHHHHHHENLYFQGMTMCDETIILNVLGQYTRAHDRRDPDAMAALFAPEATIEIVDAVGGASRSISRLEGRD
AIRVAVRQMMAPHGYRAWSQNVVNAPIIVIEGDHAVLDAQFMVFSILAAEVPDGGWPTGTFGAQGRICPIEAGQYRL
TLRTVADGWVISAMRIEHRLPMAFG

3ZEZ_INCYPRO
MGSSHHHHHHSSGLVPRGSHMASMTGGQQMGRGSMTNTLQVKLLSKNARMPERNHKTDAGYDIFSAETVVLEPQEKA
VIKTDVAVSIPEGCVGLLTSRSGVSSKTHLVIETGKIDAGYHGNLGINIKNDHEDDCMQTIFLRNIDNEKIFEKERH
LYKLGSYRIEKGERIAQLVIVPIWTPELKQVEEFESVSERGEKGFGSSGV

1VIY_INCYPRO
MASLRYIVALTGGIGSGKSTVANAFADLGINVIDADIIARQVVEPGAPALHAIADHFGANMIAADGTLQRRALRERI
FANPCEKNWLNALLHPLIQQETQHQIQQATSPYVLWVVPLLVENSLYKKANRVLVVDVSPETQLKRTMQRDDVTREH
VEQILAAQATREARLCVADDVIDNNGAPDAIASDVARLHAHYLQLASQFVSQEKPEGGSHHHHHH

7MS0_INCYPRO
MAPTYTCWSQCIRISREAKQRIAEAITDAHHELAHAPKYLVQVIFNEVEPDSYFIAAQSASENHIWVQATIRSGRTE
KQKEELLLRLTQEIALILGIPNEEVWVYITCIPGSNMTEYGRLLMEPGEEEKWFNSLPEGLRERLTELEGSSEENLY
FQGLEHHHHHH

4OZJ_INCYPRO
MGSSHHHHHHSSGLVPAGSHMSDADLPNDGGIKLVMAIIRPDKLADVKTALAEVGAPSLTVTCVSGRGSQPAKKSQW
RGEEYTVDLHQKVKVECVVADTPAEDVADAIADAAHTGEKGDGKIFILPVCNAIQVRTGKTGRDAV

4E9X_INCYPRO
MAEREFDMTIEEVTIKVAPGLDYKVFGFNGQVPGPLIHVQEGDDVIVNVTNNTSLPHTIHWHGVHQKGTWRSDGVPG
VTQQPIEAGDSYTYKFKADRIGTLWYHCHVNVNEHVGVRGMWGPLIVDPKQPLPIEKRVTKDVIMMMSTWESAVADK
YGEGGTPCNVADYFSVNAKSFPLTQPLRVKKGDVVKIRFFGAGGGIHAMHSHGHDMLVTHKDGLPLCSPYYADTVLV
SPGERYDVIIEADNPGRFIFHDHVDTHVTAGGKHPGGPITVIEYDGVPVDDWYVWKDKDYDPNFFYSESLKQGYGMF
DHDGFKGEFEQRQRRPGRKLAAALEHHHHHH

5C9G_INCYPRO (e4)
MGHHHHHHSSGVDLGTENLYFQSMTLPIRLDIAAPLAEIVLNKPERRNALSVDMWAAIPGLVAEANANPDVKLILIH
GGDAGAFAAGADISEFETIYATEDAAKASGQRIAQALDAIENSEKPVIAAIEGACVGGGVSLAMAADLRVAGEGAKF
GVTPGKLGLVYPAGDTRRLLAAVGPGATKDILFTGRIFTAGEAKCLGLIDRLVEKGTALEAARVWAGEIAAISQWSV
RATKRMIRGLQTCWTDETPEAQSLFLNGFANEDFKEGYRAFLDKRPAKFTYR

4LK5_INCYPRO

MGHHHHHHSSGVDLGTENLYFQSMPSSAIATLAPVAGLDVTLSDGVFSVTINRPDSLNSLTVPVITGIADAMEYAAT
DPEVKVVRIGGAGRGFSSGAGISADDVSDGGGVPPDEIILEINRLVRAIAALPHPVVAVVQGPAAGVGVSIALACDV
VLASENAFFMLAFTKIGLMPDGGASALVAAAVGRIRAMQMALLPERLPAAEALCWGLVTAVYPADEFEAEVDKVIAR
LLSGPAVAFAKTKLAINAATLTCLDPALQREFDGQSVLLKSPDFVEGATAFQQRRTPNFTDR

2WST_INCYPRO

MGSSHHHHHHSSGLVPRGSHMASMTGGQQGRILCYPTLWTGPAPEANVTFSGENSPSGILRLCLSRTGGTVIGTLSV
QGSLTNPSTGQTLGMNLYFDADGNVLSESNLVRGSWGMKDQDTLVTPIANGQYLMPNLTAYPRLIQTLTSSYIYTQA
HLDHNNSCVDIKIGLNTDLRPTAAYGLSFTMTFTNSPPTSFGTDLVQFGYLGQD

3GTZ_INCYPRO

MASLSIVRIDAEDRWSDVVIYNCTLWYTGVPENLDADAFEQTANTLAQIDAVLEKQGSSKSRILDATIFLSDKADFA
AMNKAWDAWVVAGHAPVRCTVCAGLMNPKYKVEIKIVAAVEGHHHHHH

1VMF_INCYPRO (b4)

MGSDKIHHHHHHMKTFHLTTQSRDEMVDITSQIETWIRETGVTNGVAIVSSLHTTAGITVNENADPDVKRDMIMRLD
CVYPWHHENDRHMEGNTAAHLKTSTVGHAQTLIISEGRLVLGTWQGVYFCEFDGPRTNRKFVVKLLCD

1KR4_INCYPRO

MGSSHHHHHHSSGREALYFMGHMILVYSTFPNEEKALEIGRKLLEKRLIACFNAFCIRSGYWWKGEIVQDKEWAAIF
KTTEEKEKELYEELRKLHPYETPAIFTLKVCNILTEYMNWLRESVLGS

5WYN_INCYPRO

MAVPSPPPASPRSCYNFIADVVEKTAPAVVYIEILDRHPFLGREVPISNGSGFVVAADGLIVTNAHVVADRRRVRVR
LLSGDTYEAVVTAVDPVADIATLRIQTKEPLPTLPLGRSADVRQGEFVVAMGSPFALQNTITSGIVSSAQRPARDLG
LPQTNVEYIQTDAAIDFGNSGGPLVNLDGEVIGVNTMKVTCGISFAIPSDRLREFLHRGEKKNSSSGISGSQRRYIG
VMMLTLSPSILAELQLREPSFPDVQHGVLIHKVILGSPAHRAGLRPGDVILAIGEQMVQNAEDVWEAVRTQSQLAVQ
IRRGRETLTLYVTPEVTEHHHHHH

Table S12. Enhanced thermal stability of bicyclic trimer designs. Circular dichroism derived T_m values for trimer designs before and after bicyclization, presented in Figure 5.

Protein	T_m / °C		
	Unreacted	Bicyclic	ΔT_m / °C
l4 (3FNJ)	61	80	19
b4 (1VMF)	77	83	6
a4 (3C6V)	41	80	39
e4 (5C9G)	54	71	17

Supplementary References

[1] Drienovská, I., Gajdoš, M., Kindler, A., Takhtehchian, M., Darnhofer, B., Birner-Gruenberger, R., Dörr, M., Bornscheuer, U.T., and Kourist, R. (2020). Folding Assessment of Incorporation of Noncanonical Amino Acids Facilitates Expansion of Functional-Group Diversity for Enzyme Engineering. Chemistry - A European Journal 26, 12338–12342. 10.1002/chem.202002077.

[2] Fürst, M.J.L.J., Martin, C., Lončar, N., and Fraaije, M.W. (2018). Experimental Protocols for Generating Focused Mutant Libraries and Screening for Thermostable Proteins. Methods Enzymol 608, 151–187. 10.1016/BS.MIE.2018.04.007.

[3] Wilkins, M.R., Gasteiger, E., Bairoch, A., Sanchez, J.C., Williams, K.L., Appel, R.D., and Hochstrasser, D.F. (1999). Protein identification and analysis tools in the ExPASy server. Methods Mol Biol 112, 531–552. 10.1385/1-59259-584-7:531.

[4] Depraz Depland, A., Stroganova, I., Wootton, C.A., and Rijs, A.M. (2023). Developments in Trapped Ion Mobility Mass Spectrometry to Probe the Early Stages of Peptide Aggregation. J Am Soc Mass Spectrom 34, 193–204. 10.1021/jasms.2c00253.

[5] Frottin, F., Martinez, A., Peynot, P., Mitra, S., Holz, R.C., Giglione, C., and Meinnel, T. (2006). The proteomics of N-terminal methionine cleavage. Molecular and Cellular Proteomics 5, 2336–2349. 10.1074/mcp.M600225-MCP200.

[6] Geoghegan, K.F., Dixon, H.B.F., Rosner, P.J., Hoth, L.R., Lanzetti, A.J., Borzilleri, K.A., Marr, E.S., Pezzullo, L.H., Martin, L.B., Lemotte, P.K., et al. (1999). Spontaneous α-N-6-phosphogluconoylation of a “His tag” in Escherichia coli: The cause of extra mass of 258 or 178 Da in fusion proteins. Anal Biochem 267, 169–184. 10.1006/abio.1998.2990.